Available online at www.sciencedirect.com
ScienceDirect
Trans. Nonferrous Met. Soc. China 29(2019) 2005−2026
Transactions of Nonferrous Metals Society of China
www.tnmsc.cn

A comparative study on microstructural evolution and surface properties of graphene/CNT reinforced Al6061−SiC hybrid surface composite fabricated via friction stir processing

Abhishek SHARMA, Vyas Mani SHARMA, Jinu PAUL

Department of Mechanical Engineering, Indian Institute of Technology, Kharagpur 721302, India

Received 30 November 2018; accepted 4 July 2019

Abstract: A comparative study on the surface properties of Al−SiC−multi walled carbon nanotubes (CNT) and Al−SiC−graphene nanoplatelets (GNP) hybrid composites fabricated via friction stir processing (FSP) was documented. Microstructural characterization reveals a more homogeneous dispersion of GNPs in the Al matrix as compared to CNTs. Dislocation blockade by SiC and GNP particles along with the defect-free interface between the matrix and reinforcements is also observed. Nanoindentation study reveals a remarkable ~207% and ~27% increment in surface nano-hardness of Al−SiC−GNP and Al−SiC−CNT hybrid composite compared to as-received Al6061 alloy, respectively. On the other hand, the microhardness values of Al−SiC−GNP and Al−SiC−CNT are increased by ~36% and ~17% relative to as-received Al6061 alloy, respectively. Tribological assessment reveals ~56% decrease in the specific wear rate of Al−SiC−GNP hybrid composite, whereas it is increased by ~122% in Al−SiC−CNT composite. The higher strength of Al−SiC−GNP composite is attributed to the mechanical exfoliation of GNPs to few layered graphene (FLG) in the presence of SiC. Also, various mechanisms such as thermal mismatch, grain refinement, and Orowan looping contribute significantly towards the strengthening of composites. Moreover, the formation of tribolayer by the squeezed-out GNP on the surface is responsible for the improved tribological performance of the composites. Raman spectroscopy and various other characterization methods corroborate the results.

Key words: friction stir processing; graphene; carbon nanotube; hybrid composite; wear

1 Introduction

Aluminium matrix composites (AMC) are the high-performance materials for the extensive range of applications owing to their excellent combination of properties such as higher strength, stiffness, and wear resistance compared to the unreinforced alloys [1]. AMCs can be fabricated by various methodologies like liquid infiltration [2], powder metallurgy [3], and stir casting [4]. All these processes improve the bulk properties of the base materials and generally involve high temperature, which promotes the formation of oxides and intermetallics. On the other hand, several other applications require improved surface properties of the composite, keeping the bulk properties of the base material intact. Recently, friction stir processing (FSP) has been developed, as a solid state process, based on the friction stir welding technique to produce surface metal matrix composites.

The surface composites fabricated by FSP using SiC as reinforcements have shown a significant improvement in surface hardness [5,6]. Furthermore, incorporation of SiC significantly increases the wear resistance of the surface composites [7]. The improved tribological and mechanical properties by SiC reinforcement were attributed to the grain refinement during FSP, homogeneous dispersion of SiC, and the higher hardness of abrasive SiC particles. The volume fraction and particle size of SiC also significantly contribute towards the improved surface properties of the fabricated composite.

Among various reinforcements, carbonaceous materials such as graphite, graphene, and carbon nanotubes (CNTs) are the excellent candidates due to their high thermal conductivity, lower coefficient of thermal expansion, and self-lubricating properties. The mono composite of Al−graphene, fabricated through FSP, increases the thermal conductivity without sacrificing the ductility of the composite [8]. MAURYA et al [9]

Corresponding author: Jinu PAUL; Tel: +91-3222282956; E-mail: jinu.paul@mech.iitkgp.ac.in
DOI: 10.1016/S1003-6326(19)65108-3

observed around 160% increase in the surface hardness and 84% increase in wear resistance by reinforcing graphene in the Al matrix. DIXIT et al [10] reported a two-fold increase in the strength of the composite by exfoliation of graphite into multi-layer graphene during FSP. KHODABAKHSHI et al [11] also reported 55% and 220% increase in hardness and tensile strength of Al−graphene composite fabricated through FSP, respectively.

Similarly, CNT also serves as an excellent reinforcement when incorporated into the Al matrix via FSP. The CNT reinforcements have significantly increased the strength of the composite in previous study [12]. IZADI and GERLICH [13] reported the destruction of the tubular structure of CNT during FSP along with the 100% increase in the surface microhardness of the composite. LIU et al [14] reported the change in structure from ductile to brittle on increasing the CNT content above an optimum level. LIM et al [15] reported a non-uniform dispersion of CNT in the Al matrix due to its entangled morphology. Likewise, Al−graphite mono composite also shows an increased wear resistance due to the formation of a rich layer of lubricant during FSP [9]. This continuous solid graphite-rich layer provides solid lubrication and prevents interaction between two metallic surfaces and consequently decreases the frictional resistance and wear.

Hybrid aluminium matrix composites are fabricated by reinforcing two or more different types of particles in the Al matrix. Hybrid surface composites reveal better properties than the mono composites [16]. Al−SiC−graphite hybrid composite fabricated by FSP displays an increased wear resistance [17]. The SiC and graphite act as a load-bearing element and solid lubricant, respectively, in the Al matrix. SHARMA et al [18] demonstrated the increase in nano-hardness of the Al−SiC−graphite hybrid surface composite along with the change in graphite morphology when fabricated by FSP. TANG et al [19] conducted the molecular dynamics based simulations for evaluating the effect of encapsulating graphene on the strength of Al−SiC composites. They claimed to have a significant increment in the strength of Al−SiC−graphene nanoplatelets (GNP) composite due to various micro-scale strengthening mechanisms. Similarly, ZENG et al [20] fabricated Al−SiC−reduced graphene oxide (RGO) hybrid composite by powder metallurgy route. Here, they reported that hybrid Al−Si/SiC_p/RGO composite possesses the low wear rate because of the stabilized COF, and the self-lubricating effects of incorporated RGO. Similarly, SENEL et al [21] observed around 200% increment in Vickers hardness and 155% increment in the overall strength of Al−SiC−GNP composite as compared to aluminium. Here also, they have fabricated the composite by using powder metallurgy route. Recently, ZHAN et al [22] found that graphene mainly has two effects on the mechanical properties of hybrid composites. One is to improve the bonding performance of the particle− matrix interface and thus facilitate the force transmission. Another one is the enhancement of the elastic modulus and the tensile strength as well as the loss of ductility. The study of Al−SiC−CNT is till now conducted only by HEKNER et al [23]. Here also, they have fabricated composite with powder metallurgy (PM) route and reported a considerable improvement in the wear resistance of the composite.

The noteworthy point here is that, all the above researchers have utilized a powder metallurgy route for the fabrication of Al−SiC−GNP/CNT hybrid composite. However, manufacturing of a component through the PM route involves at least three critical steps: powder blending, compaction, and sintering. Overall, the PM route takes 4 to 8 steps to get the final product. Moreover, it requires a considerable amount of capital investment to perform every step of the manufacturing process via the PM route. The high-temperature sintering also involves the formation of various reaction products, including Al_4C_3, which are detrimental to the composite strength. An alternative to this, FSP is a rapid, cost- effective, and environmental friendly approach for composite manufacturing. The plastic deformation during FSP provides an additional strain hardening to the composite other than the strengthening produced by the reinforcements. Hence, the present study aims to take advantage of the plastic deformation and strengthening mechanism provided by the reinforcements such as graphene, CNT, and SiC by fabricating a hybrid composite through FSP. For comparison, mono composites of Al−GNP, Al−CNT, and Al−SiC are also fabricated. The effects of various reinforcements and FSP on the microstructure, micro/nano-mechanical behavior, and wear resistance of the composites were investigated in detail.

2 Experimental

2.1 Materials and processing

Commercially available Al6061 aluminium alloy plate of 5 mm in thickness was used as a substrate or base metal (BM) in the present study. Table 1 presents the chemical composition of the base Al6061 alloy. GNP (United Nanotech Innovations, India) of 5−10 nm in thickness with 5 μm lateral dimension and 3−10 layers was used as one of the reinforcements. CNTs (United Nanotech Innovations, India) of outer diameter ~25 nm and length 1−10 μm with ~12 layers were used as another carbonaceous reinforcement. Silicon carbide

(SiC) (Alfa Aesar) of 30 μm in size was used as a ceramic reinforcement. The microstructure and morphology of various raw materials are illustrated in Fig. 1.

Table 1 Chemical composition of base AA6061 aluminium alloy (wt.%)

Mg	Si	Fe	Cu	Ti	Zn	Mn	Cr	Al
0.9	0.6	0.4	0.25	0.10	0.15	0.05	0.10	Bal.

A groove of dimensions 3 mm × 3.5 mm (width × depth) was fabricated in Al6061 base metal by using an end milling machine. The grooves are filled with a paste of SiC, GNP and CNT for mono composites whereas with a paste of SiC−GNP (1:1) and SiC−CNT (1:1) for the hybrid composite. FSP was carried out on the surface opposite to the surface on which grooves are fabricated. This method prevents the reinforcement from escaping out of the grooves during the centreline motion of the tool pin. The FSP was conducted on a numerically controlled friction stir welding setup (ETA technology, India) by using a tool made up of H-13 hardened steel of dimensions 24 mm in shoulder diameter, 6 mm in pin diameter, and 4.5 mm in pin length. From the results of our previous work [18], the best rotational speed of 2200 r/min with 25 mm/min traverse speed, 0.2 mm plunge depth, and the 2° tool tilt angle are revised for the present study. Temperature study was carried out by using K type thermocouple attached at a distance of 3 mm away from the processing zone. Figure 2 shows the schematic representation and experimental setup of FSP.

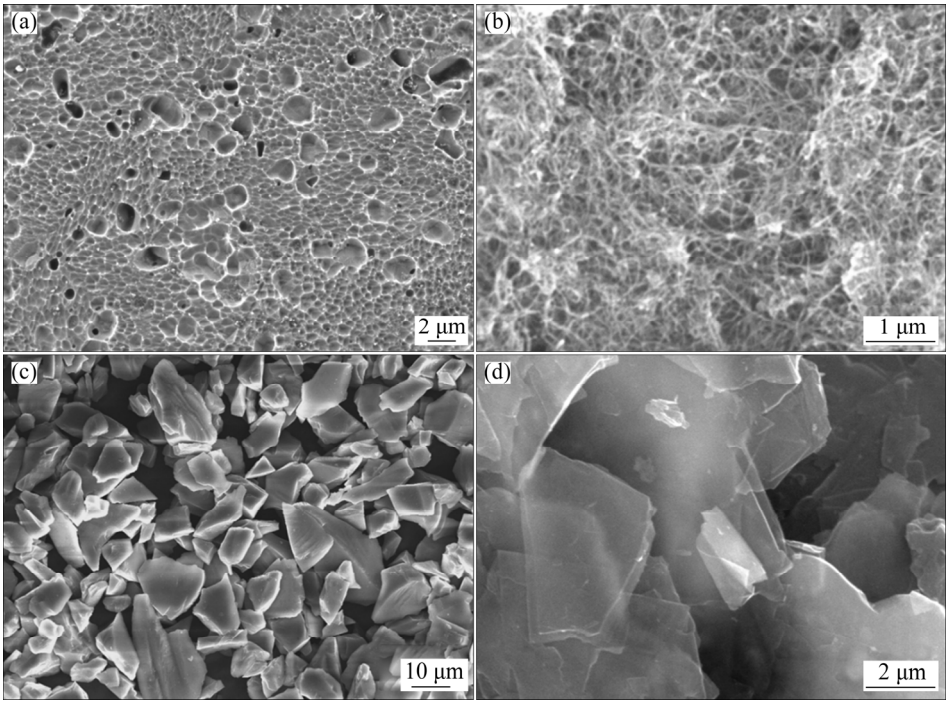

Fig. 1 Microstructure and morphology of as-received Al6061 (a), multi-walled CNT (MWCNT) (b), SiC (c) and GNP (d)

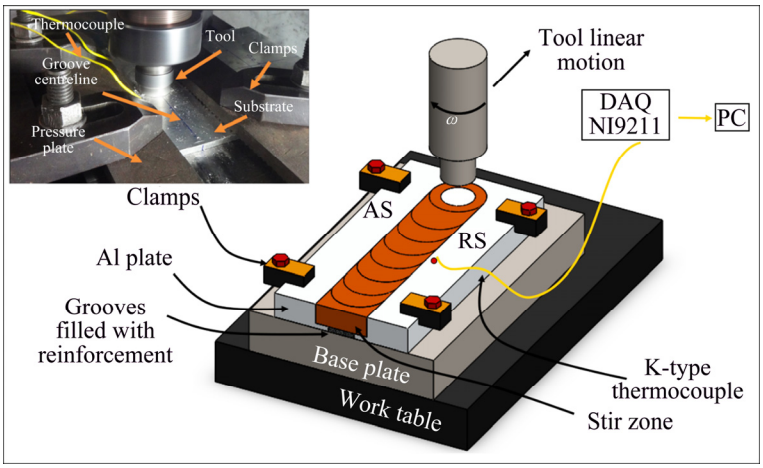

Fig. 2 Schematic representation of FSP setup (Inset shows experimental setup)

2.2 Microstructural characterization

Microstructural characterization of the fabricated hybrid and mono composites was carried out by using field emission scanning electron microscope (FE-SEM) (Merlin, Zeiss (Germany)) integrated with EDAX detector. For microstructural analysis, samples were primarily polished with abrasive papers (220, 400, 600, 800, and 1200 grit size). It is then fine cloth polished using a HIFIN diamond paste (Geologist's syndicate, India). Finally, the samples were etched by using Keller's reagent (90 vol.% distilled water, 5 vol.% HNO_3, 3 vol.% HCl, and 2 vol.% HF). The phase characterization was carried out by using X-ray diffraction (XRD) PANalytical (EMPYREAN, DY1705)). Raman spectroscopy (Jobin Yvon Horiba, T64000) was used for the morphological analysis of carbonaceous compounds before and after FSP. The raw data obtained using Raman spectroscopy were firstly smoothened to 5 points by using Savitzky−Golay function in Origin 8.5 software. Later, a baseline correction was carried out by using Gaussian distribution.

2.3 Mechanical and tribological properties

The nano- and micro-mechanical behaviors of the fabricated composites were evaluated by using nanoindentation (Hystiron, TI 950) and Vickers microhardness (Omnitech, S.Auto) tests, respectively. The flat samples for hardness test are acquired from the center of the traversing length by using wire electrical discharge machining (EDM). The nanoindentation with a load of 5 millinewton was made on the transverse side of the samples in a matrix form (5 points × 7 rows) with the first row at a distance of 50 μm from the surface. The distance between the consecutive points in a row and column is 50 μm each. Vickers microhardness was also carried out on the cross-section surface with a load of 200 g. The microhardness readings were taken at an equal interval of 0.5 mm in both the advancing side (AS) and retreating side (RS). The loading, dwell, and unloading time of 10 s each was used for both the hardness methods.

Tribological properties were assessed by the dry sliding wear test conducted through a ball on disc wear test machine (Ducom, TR-208-M1). The wear was conducted on the processed surface, and the samples were initially smoothened by manual paper polishing to remove the surface asperities created due to processing. The test was carried out in the air at room temperature. The normal load applied during the testing was 20 N at a speed of 20 r/min. The track radius was fixed to 2 mm. The test was conducted for 20 min making a linear sliding distance of ~5 m. Wear test was carried out by the steel balls used in ball bearings.

3 Results and discussion

3.1 Heat generation and surface profile

Figure 3 shows the variation of peak temperature during FSP with various reinforcements. The following significant information can be obtained from these curves: (1) The peak temperature obtained by various reinforcements is well below the melting point of the Al alloy indicating solid-state processing; (2) The peak temperature, heating rate and cooling rate critically govern the grain size; and (3) The time for which the material is exposed to the temperature above the recrystallization temperature.

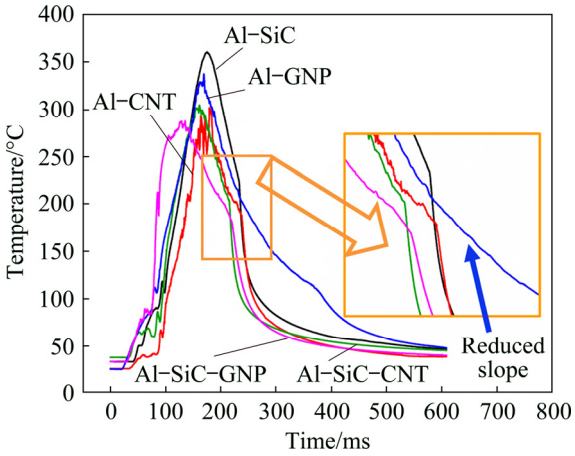

Fig. 3 Temperature profile obtained during FSP of various composites (Inset shows zoom-up image of marked region)

As seen in Fig. 3, the peak temperature of various composites fabricated by FSP is in the range of ~260 to ~360 °C. Thus the obtained peak temperature is far below the melting point of aluminium (~660 °C). The heating rate is almost identical for all the fabricated composites as seen from the slope of the heating region of the thermal curves. However, there is significant variation in the cooling rate of CNT and GNP reinforced composites. The mono composite of GNP displays a higher cooling rate, up to ~200 °C, and then the cooling rate decreases, which is evident from the decreased slope of the curve. This phenomenon is attributed to the remarkably high thermal conductivity of GNP, which increases the cooling rate/heat transfer at higher temperature gradient. As the temperature decreases up to 200 °C, the temperature gradient between the substrate and the atmosphere also reduces. This reduced temperature gradient ultimately decreases the cooling rate and results in the reduced slope of the Al−GNP fabricated composite. The recrystallization temperature of alloy generally lies in the range $0.4T_m$ to $0.5T_m$ (where T_m is the melting temperature). For aluminium this range

exists between 264 and 330 °C. As evident from the thermal curves, this temperature range exists only for the short duration (~40 s) for various composites. Thus, due to this short exposure time, the probability of grain growth also decreases.

Figure 4 presents the Al surface obtained after FSP with various reinforcements. The mono composites of Al−GNP, Al−CNT, and Al−SiC display a characteristic tunneling defect in the advancing side (AS). This tunneling defect mainly appears due to insufficient plasticization of the materials and non-uniform material movement around the tool pin. The graphene exhibits an exceptionally higher thermal conductivity of 2000−4000 W/(m·K) [24]. Due to this high thermal conductivity, the heat generated in the stir zone rapidly conducted to the adjacent surfaces. Consequently, the absence of proper temperature in the processing zone results in the insufficient plasticization of the material. This insufficient plasticization also increases the flow stress of the material, causing deficient material movement, which hampers its consolidation leading to the tunneling defect on the advancing side [25]. Moreover, the flow shear stress experienced due to insufficient plasticization during FSP is higher than the interlayer shear strength (~0.48 MPa) of GNP. This phenomenon leads to the shearing of GNP interlayers to form a carbon-rich solid lubricant layer at the tool/substrate interface [10]. The GNP based solid lubricant layer adversely affects the loading condition, and seizure could not take place during processing and ultimately affects the material flow.

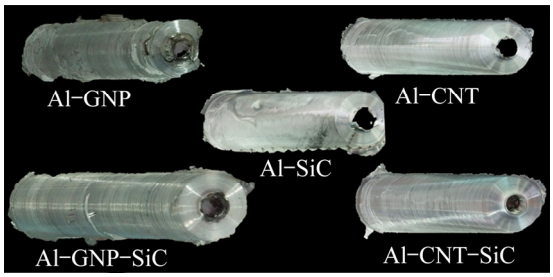

Fig. 4 Surface profiles of various composites after FSP

As mentioned earlier, the FSP was carried out on the surface opposite side of the grooves. Thus, the aluminum surface in contact with the tool shoulder is not having any discontinuity up to 1.5 mm as measured on the cross-section. Also, due to higher friction generated between the tool shoulder and Al plate, this region has higher heat generation as compared to the bottom section of the plate where the groove is fabricated. As a result, the bottom zone of the plate suffers from the insufficient plastic flow of the Al matrix, as shown schematically in Fig. 5. Also, the downward material flow reduces significantly due to the presence of a 1.5 mm-thick Al layer at the top. Moreover, the plastic flow is obstructed due to the presence of hard SiC abrasive particles in the matrix [26]. The combined effect of all the phenomenon mentioned above results in the inability of the material to flow from the retreating side (RS) to the advancing side (AS) and consequently to fill the groove zone.

A similar mechanism explains the tunneling defect on AS in Al−CNT mono composite. However, the hybrid composites are free from any such defect and also display an excellent surface finish. In Al−SiC−GNP and Al−SiC−CNT hybrid composites, SiC particles compensate the interlayer shearing effect of GNP, causing the seizure and uniform axial force conditions during processing. Thus, the defect-free processing zone in hybrid composites is attributed to the presence of hard abrasive SiC particles in the matrix.

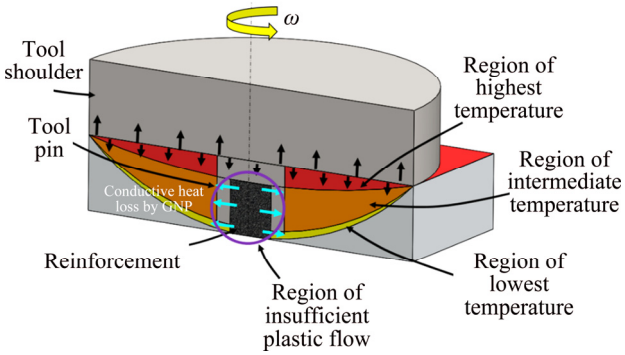

Fig. 5 Schematic representation of heat flow during FSP

3.2 Microstructural evolution

Figures 6(a−c) show the FE-SEM micrographs of the fabricated Al−CNT, Al−GNP, and Al−SiC mono composites, respectively. The SEM micrographs visualize the CNT agglomerates with a drastic change in the morphology and size of CNT particles. The CNTs in the composite were shorter than the as-received ones due to significant stirring and breakup during FSP. The fracture in CNTs can also be confirmed by the presence of open ends in the CNT structure. Similar open-ended morphology of CNT was also visualized by LIM et al [15]. The entangled CNTs were firstly cut-off by the shear effect during FSP. The fragmented particles are then subsequently dispersed in the Al matrix due to the plastic flow of aluminium. The agglomerates of CNTs are attributed to the entangled behavior of the as-received CNTs and the ineffectiveness of the single pass FSP to disperse the particles in the matrix. EDAX analysis confirms the identity of CNTs in the Al matrix.

Similarly, agglomerates of the GNPs are also observed in the fabricated Al−GNP mono composite, as shown in Fig. 6(b). The GNPs are entrapped in the defect sites created by the improper flow of material during FSP, as shown in Fig. 6(b_1). The presence of wrinkled

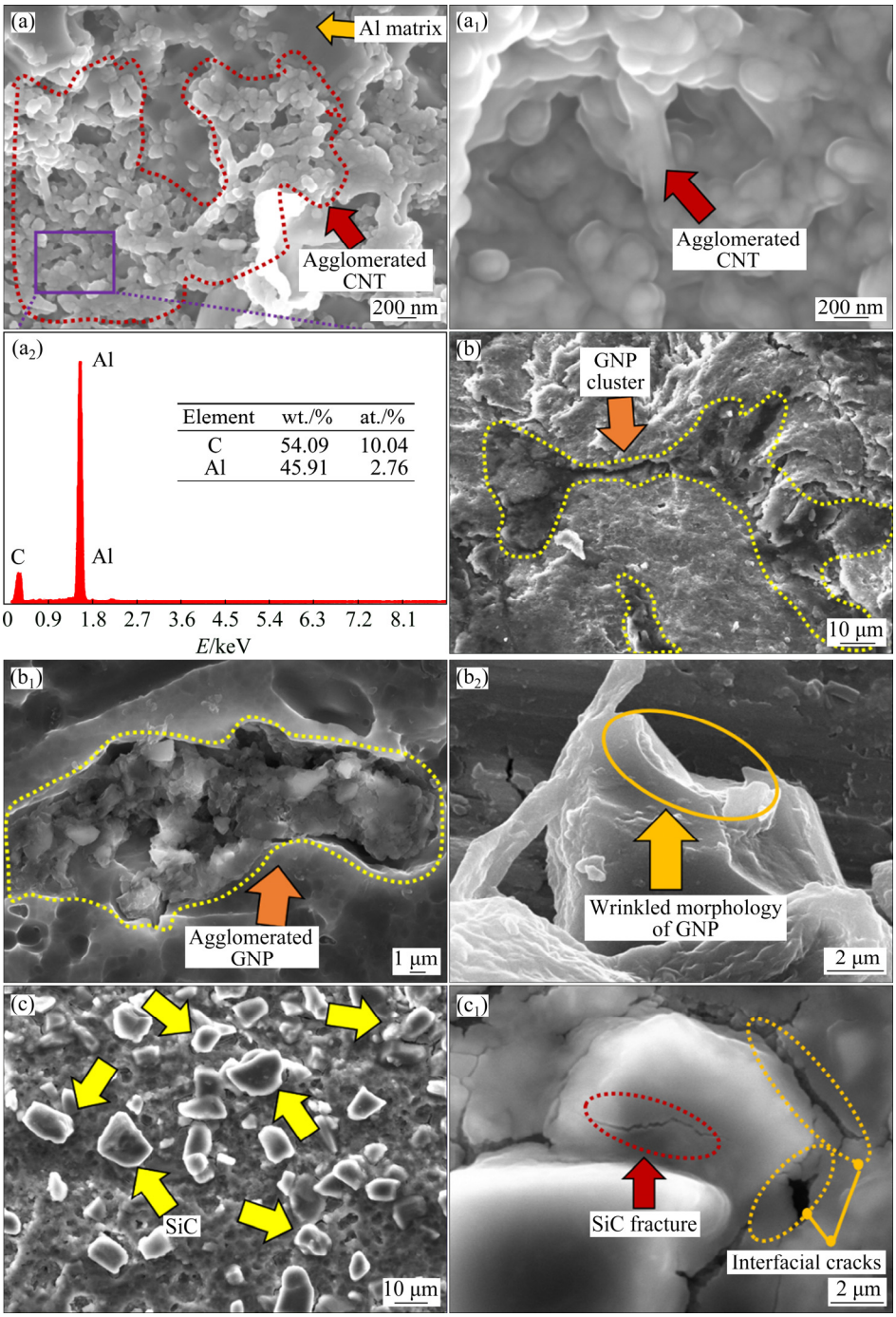

Fig. 6 SEM micrographs and EDS result of fabricated mono composites: (a, a_1, a_2) Al−CNT; (b, b_1, b_2) Al−GNP; (c, c_1) Al−SiC (Figures (a_1, b_1, b_2 and c_1) present higher magnification images of corresponding samples while Fig. (a_2) shows EDS analysis of relevant section in (a))

morphology of the GNP even after severe plastic deformation during FSP is the remarkable feature as illustrated in Fig. 6(b_2). The agglomerates mainly arise due to improper flow of material around the groove zone owing to the high thermal conductivity of GNP as discussed earlier in Section 3.1. Also, the high aspect ratio of graphene restricts the flow of GNP along with the flow of matrix material [9].

Figure 6(c) depicts the SEM micrograph of the fabricated Al−SiC mono composite. The fragmented and uniformly distributed SiC particles can be visualized from the SEM micrographs. The high magnification micrograph illustrated in Fig. 6(c1), represents the crack formation on the SiC particle due to the intense stirring during FSP. The crack initiation and propagation in SiC particles result in the fragmented particles which are more homogeneously distributed in the Al matrix. Moreover, the high magnification image (see Fig. 6(c_1))

also shows the interfacial crack formation in the vicinity of SiC particles. These interfacial cracks are detrimental to the mechanical properties as well as for the corrosion resistance of the composite [27]. The interfacial cracks are attributed to the slower relaxation of the stress and strain built-up at the interface, due to much more difficult thermal activated deformation during FSP [28].

Figure 7 shows the SEM micrographs of the fabricated Al−SiC−GNP hybrid composite. Figure 7(a) visualizes the homogeneous dispersion of both SiC and GNP particles in the Al matrix. The distribution of SiC and GNP in the aluminium matrix can also be visualized from Fig. 7(b). However, the GNP particles are mostly dispersed in the vicinity of SiC particles. Figures 7(b_1, b_2) represent the higher magnification images of the composite. The exfoliation of GNP into FLG can be visualized from Fig. 7(b_2). During the flow of reinforcement with the matrix material, the hard SiC particles restrict the movement of GNP with the material flow [18]. This obstruction increases the strain experienced by GNP, and consequently, the flow stress acting on the GNP starts rising. Up to the threshold value, i.e., the interlayer shear strength of GNP (~0.47 MPa), the flow stress tends to increase and as soon as the stress threshold value is reached, the GNP starts exfoliating into few-layer graphene which is represented in Fig. 7(b_2). Another unique feature observed in Al−SiC−GNP hybrid composite is the filling of the interfacial crack between the Al matrix and SiC by GNP particles. The GNP particles act as a bridge between the Al matrix and SiC particles, as shown in Fig. 7(b_1). The bridging mechanism is also confirmed by using TEM analysis and discussed later in this work. The encircled region (red) represents the excellent interface between the Al matrix and SiC particles. The GNP pulled out by SiC can also be visualized in the encircled area (yellow) which shows the flow restricting motion of GNP by the SiC particles. Figure 7(c) shows the EDS elemental mapping of the fabricated hybrid composite.

Figure 8 shows the SEM micrographs of Al−SiC−CNT hybrid composite. The uniform dispersion of fragmented SiC particles can be visualized from Figs. 8(a) and (a_1). Also, the clusters of CNTs in the Al matrix are not present in the hybrid composite which was earlier seen in Al−CNT mono composite (Figs. 6(a, a_1)). Moreover, some single dispersed CNTs in the Al matrix can be visualized from the SEM micrographs. The CNT particles are believed to be broken down during FSP, which was also reported in the earlier studies [28]. Figure 8(b) represents the high magnification images of CNT particles freely rested in Fig. 8(a_1), indicating that the ends of CNTs are damaged due to high shear stresses experienced during FSP. The damage of CNTs under the effect of high temperature and pressure is widely reported by various researchers [29]. The destruction of CNT walls leads to the generation of various defective structures like cap formation, partial collapse of the tube, kink, and carbon onion like graphitic structure [9]. The damaged ends also show the delamination of tube walls due to the partial crushing of CNT during FSP. These totally or partially crushed CNTs contribute towards the formation of a thin lubricating carbon film, which assists in the reduction of wear rate [30]. Figure 8(b_1) represents the diffusion of single dispersed CNTs in the Al matrix, which was not visible earlier in the Al−CNT mono composite. The CNT has poor wettability with aluminium, and thus, its diffusion in the Al matrix for the excellent interface is a tedious task. On the other hand, SiC has a far better wettability with aluminium. Thus, the adhesion between the reinforcements may have increased

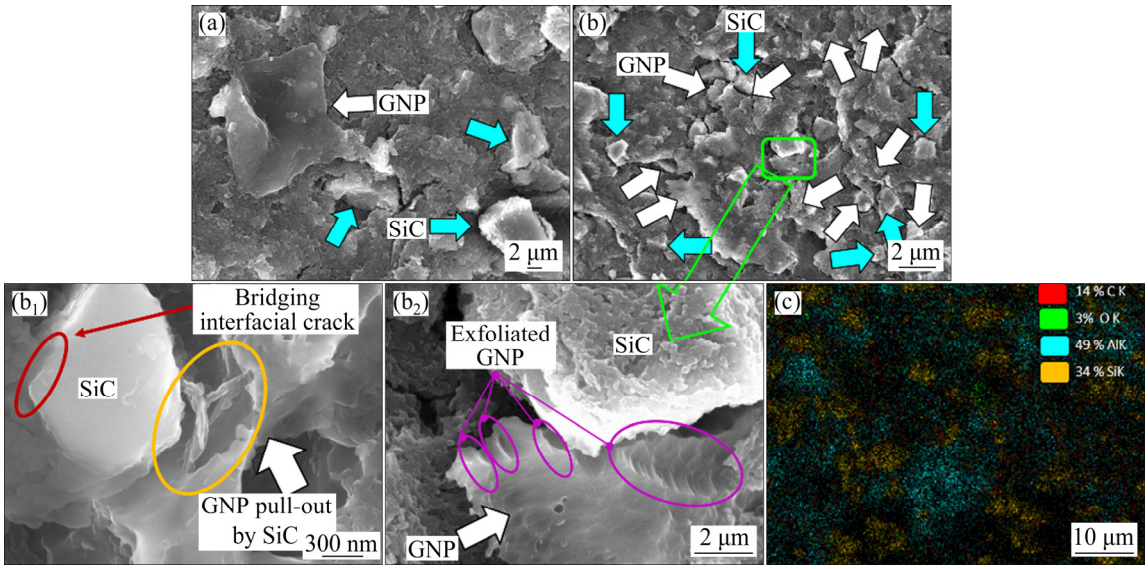

Fig. 7 SEM micrographs of Al−SiC−GNP hybrid composite: (a, b) Distribution of SiC and GNP in composite; (b_1, b_2) High magnification micrographs of (b); (c) EDS elemental mapping

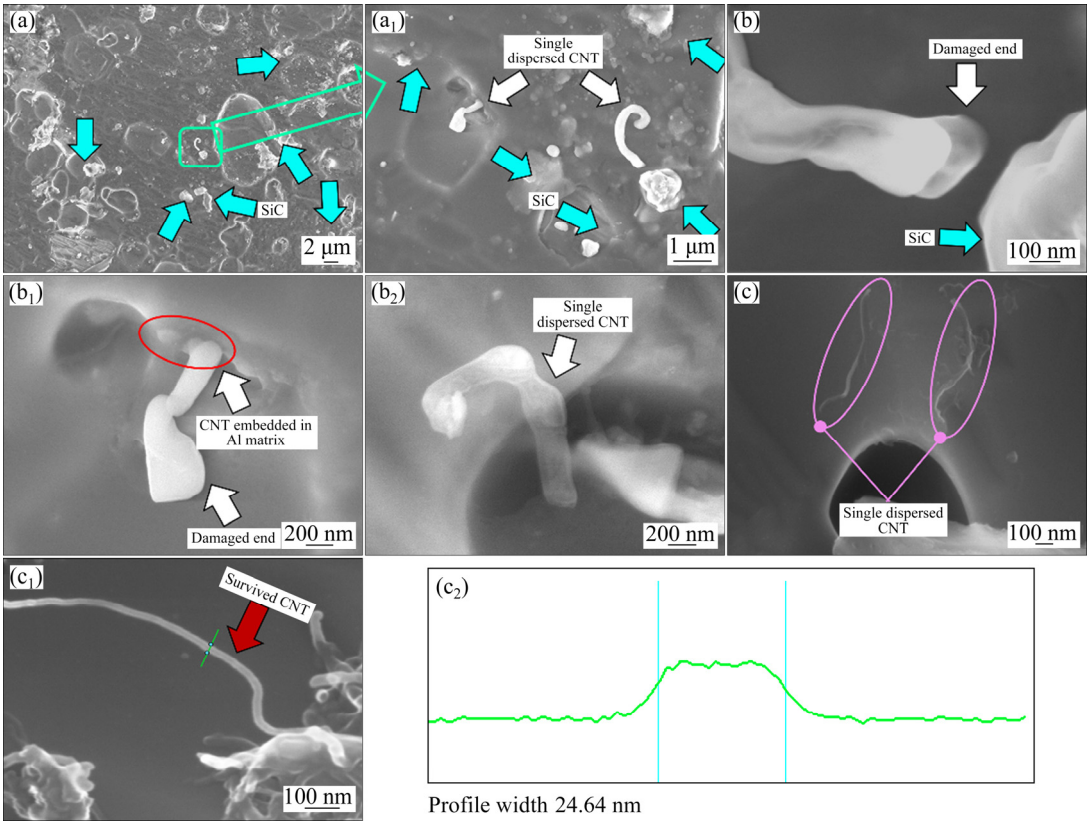

Fig. 8 SEM micrographs of Al−SiC−CNT hybrid composite: (a, a_1) Distribution of SiC and CNT in composite; (b, b_1, b_2) High magnification micrographs revealing distorted morphology of CNT; (c, c_1) Survived single dispersed CNT; (c_2) Profile width (outer diameter) measurement of survived CNT shown in (c_1)

when both CNT and SiC are present in the Al matrix, which results in the diffusion of CNT particles in Al matrix in the region nearer to SiC particles [28]. In other words, the SiC provides a platform for the CNT to diffuse in the Al matrix by increasing the wettability of reinforcement with aluminium. The SEM micrograph in Fig. 8(b_2) demonstrates the shortening of CNTs during FSP. Though the stirring action during FSP is intensive enough to shorten and distort the CNTs structure, some of the CNTs have survived the intense stirring and retained its shape and size as shown in Figs. 8(c) and (c_1).

3.3 Phase analysis

Figure 9 presents the XRD patterns of composites fabricated with various reinforcements. The peak around the 2θ angle of 26.5° corresponds to the (002) plane of carbon. The presence of this peak in GNP-reinforced Al matrix, confirms the presence of graphene in the composite. However, this peak is not observed in the composites reinforced with CNT particles. The shortening and dispersion of CNT in the Al matrix are the primary reasons for the non-appearance of the carbon peak in CNT-reinforced composites [31]. The peak around an angle of 35.65° corresponds to (111) plane of SiC. Another prominent peak of SiC appears around the

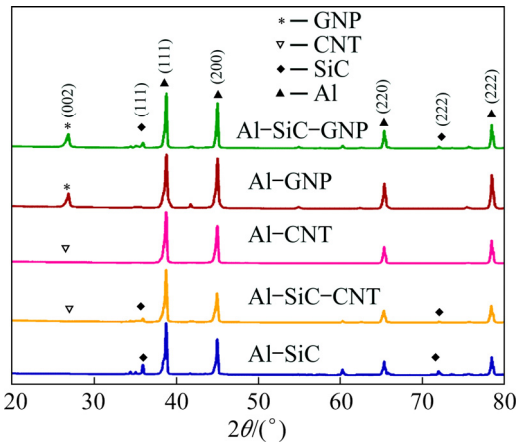

Fig. 9 XRD patterns of composites fabricated with various reinforcements

2θ angle of 74.8° which corresponds to (222) plane of SiC. Since the volume fraction of carbonaceous reinforcement and SiC in the matrix is low as compared to the Al, the peaks corresponding to the reinforcement are very weak.

The fabrication of composites via FSP involves high shear deformation at a significantly higher temperature. The treatment of material at such high temperature under the effect of severe strain leads to the reaction between

the base metal and the reinforcements resulting in the formation of intermetallic compounds. Among various reaction products, Al_4C_3 is the most harmful and possible intermetallic compound, which is generally formed at the interface of the Al matrix and carbonaceous reinforcement. Also, the open ends of CNT are the potential sites for the formation of Al_4C_3. However, the XRD pattern in Fig. 9, confirms the absence of any such intermetallic compounds in the composite. This phenomenon is attributed to the insufficient temperature generation for the kinetics of Al_4C_3 formation to get started. Various researchers [24] reported the absence of Al_4C_3 formation when the fabrication of composite is carried out at a temperature lower than ~500 °C. This effect presents an additional advantage of FSP over other alloying techniques, which involves high-temperature processing such as casting, thermal spraying and laser beam processing, etc.

3.4 Raman spectroscopy

Figures 10(a, b) provide the Raman spectra of the as-received powders, whereas, Figs. 10(c, d) show the Raman spectra of the fabricated composites. In Fig. 10(a), typical D-band (from defect and amorphous carbon), G-band (from graphite), and 2D band (shape of the second order Raman bands) of graphitic carbons are detected at a Raman shift of ~1343, ~1569, and ~2695 cm^{-1} in as-received powders, respectively. The lower intensity ratio (I_D/I_G=0.47) indicates the lower defect density in as-received GNP [32], whereas the intensity ratio I_{2D}/I_G indicates towards the degree of graphitization or the number of graphene layers [33].

In Al−GNP mono composite (see Fig. 10(c)), the peak positions of D-band, G-band, and the 2D band are shifted by ~6 cm^{-1} while the intensity ratio I_D/I_G increases from 0.47 in as-received GNP to 0.92 in Al−GNP mono composite. The peak position of the G-band corresponds to the stress states in the GNP. Under severe strain conditions during FSP, the interatomic distance of graphene changes, which in turn changes the vibrational frequency of G-band and leads to the shifting of wave number [34]. The increase in I_D/I_G ratio is attributed to compressive residual stress during FSP, and defects induced during processing. Under severe straining conditions during FSP, the interlayer distance of the consecutive GNP layers changes and results in the setup of compressive residual stresses [35]. Under the effect of these compressive residual stresses, the hexagonal symmetry of the GNP gets distorted and results in the decrease of G-band intensity as compared to as-received GNP. On the other hand, the distortion in the hexagonal symmetry of GNP is also accompanied by the generation of disorder, especially the edge disorder, which increases the D-band intensity of the Raman

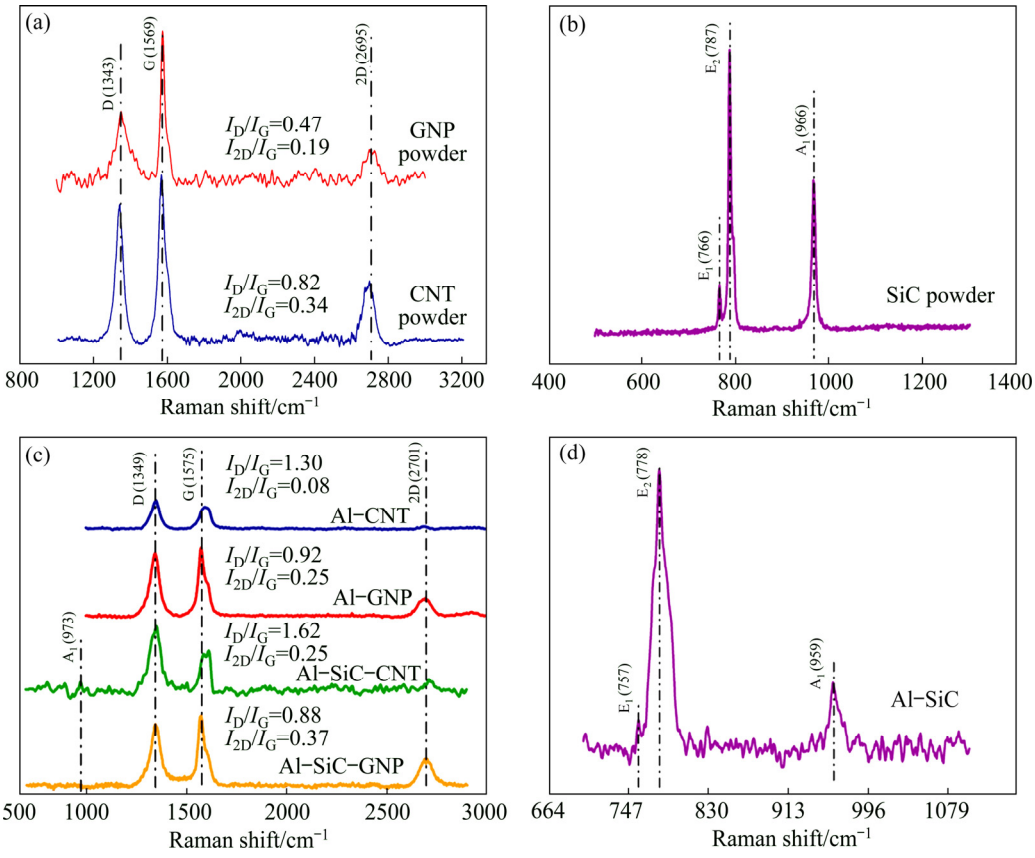

Fig. 10 Raman spectra of as-received powders (a, b) and fabricated composites (c, d)

spectra. The overall effect leads to an increase in the intensity ratio I_D/I_G. In Al−GNP mono composite, the intensity ratio I_{2D}/I_G is also increased from 0.19 in as-received GNP to 0.25 in Al−GNP mono composite. The increase in I_{2D}/I_G is attributed to the exfoliation of GNP to FLG. During FSP, the aluminium matrix and GNP go through a plastic deformation under the effect of high flow stress. Since the layer between GNPs possesses a very low interlayer shear strength (~0.48 MPa), it cannot resist the high flow shear stresses due to the plastic flow of material [36]. The ultimate effect is the separation of graphene layers from each other, which increases the intensity ratio I_{2D}/I_G.

Similar to Al−GNP mono composite, the intensity ratio I_{2D}/I_G also increases for Al−SiC−GNP hybrid composite relative to the as-received GNP. Also, the magnitude of intensity ratio is more significant than that in Al−GNP mono composite. The higher I_{2D}/I_G ratio as compared to Al−GNP mono composite is attributed to the presence of SiC in the matrix. As explained in Section 3.2, the SiC offers a resistance to the flow of GNP during the plastic flow of material. When the shear stress was exerted on the GNP due to the presence of SiC exceeds the interlayer shear strength of GNP (~0.48 MPa), the exfoliation of GNP to FLG takes place. Since, in the Al−SiC−GNP hybrid composite, the shear stress due to plastic flow and resistance by SiC both takes place, the extent of exfoliation is significantly greater than the Al−GNP mono composite and results in higher I_{2D}/I_G ratio as compared to that of Al−GNP mono composite. The exfoliation of GNP due to blockade by SiC can also be visualized in Fig. 7(b_2). The intensity ratio I_D/I_G also increases from 0.47 in as-received GNP to 0.88 in Al−SiC−GNP hybrid composite. However, it is lower than the I_D/I_G ratio obtained in Al−GNP mono composite. The similar behavior was also obtained by SHARMA et al [18] in the case of Al−SiC−graphite hybrid composite. The lower I_D/I_G ratio in Al−SiC−GNP hybrid composite is attributed to the resistance in the disorder generation (in GNP) due to the presence of SiC in the matrix. The deformation of GNP, especially the edge disorder reduces to a greater extent due to the hard abrasive property of SiC present in the matrix. With the reduction in disorder, the I_D/I_G ratio also decreases as compared to Al−GNP mono composite.

The intensity ratio I_D/I_G increased from 0.82 in as-received CNT to 1.30 and 1.62 in Al−CNT mono composite and Al−SiC−CNT hybrid composite, respectively. The increase in peak intensity ratio indicates a higher degree of structural defects in the CNT morphology. As explained earlier in this section, the increased defect density is attributed to the distortion in hexagonal symmetry under the effect of severe strain during FSP. However, the highest I_D/I_G ratio for Al−SiC−CNT is due to the delamination of tube walls and damaged ends (Fig. 8(b_2)). The I_{2D}/I_G ratio shows a reverse trend in Al−CNT mono composite while it increases in Al−SiC−CNT composite. The increase of I_{2D}/I_G ratio in Al−SiC−CNT hybrid composite is attributed to the delamination of tube walls and smearing of CNT walls under the effect of high shear stresses during FSP. Whereas, the significant reduction in the I_{2D}/I_G ratio of Al−CNT mono composite is attributed to the agglomeration and clustering of CNT as visualized from Fig. 6(a).

The Raman spectra of SiC powder show three characteristic features: The peaks of E_2 symmetry at ~766 and ~792 cm^{-1} correspond to TO(Γ) phonon or transverse optic mode, and the low-intensity peak of A_1 ~972 cm^{-1} corresponds to LO(Γ) phonon or longitudinal optic mode. These three characteristic features confirm the presence of SiC in 6H−SiC polytypes. The high-intensity peaks E_1 and E_2 correspond to the Si—C bond, while the A_1 peak represents the second order band of silicon [37]. The characteristic Raman peaks are not visualized in the hybrid composites due to the high intensity of the G-band and D-band of carbonaceous compounds. Due to this effect, the SiC peaks are indistinguishable from the noise.

3.5 Nano and micro-mechanical behavior

The fabricated composites are reinforced with nano-sized carbonaceous compounds and their effect at the very local level is significant for the strengthening, which can be analyzed through nanoindentation. Figure 11(a) presents the results obtained from the load−displacement curve by using the Oliver and Pharr method, whereas, Fig. 11(b) shows the load−displacement curves for the various fabricated mono and hybrid composites. The difference in the hardness of various samples is clear from the maximum penetration depth and elastic recovery after unloading as represented in the load−penetration curve shown in Fig. 11(b).

As seen in Fig. 11(a), the nano-hardness of the Al6061 alloy increased with the FSP as well as with the reinforcement addition. However, the increase in nano-hardness due to FSP alone in processed Al alloy is very less (~14%) and almost insignificant. The increase in hardness of processed Al6061 alloy is attributed to the grain refinement due to plastic deformation during FSP [38]. The Al−SiC, Al−GNP, and Al−CNT mono composites show an increase in nano-hardness of ~183%, ~113%, and ~27% respectively as compared to as-received Al6061 alloy. The remarkable increase in nano-hardness of ~207% is obtained in Al−SiC−GNP hybrid composite, whereas, the nano-hardness of Al−SiC−CNT composite increased only by ~47% as compared to as-received Al6061 alloy.

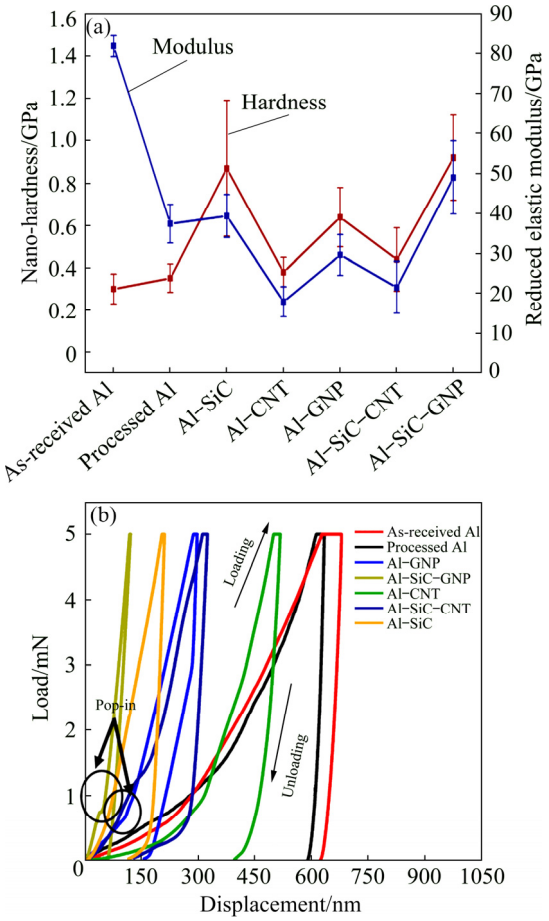

Fig. 11 Curves of nano-hardness and elastic modulus (a) and load−displacement (b)

Figure 11(a) also represents the variation in reduced elastic modulus of various samples. The reduced elastic modulus takes into account both the sample and indenter's elastic modulus and the Poisson ratio. The unloading profile of the load−depth curve is generally used to calculate the reduced elastic modulus of the sample [39]. The slope of the unloading profile can directly be inferred as the elastic modulus of the given sample. According to SAHOO et al [32], if the depth of penetration in the sample is more, lesser will be the elastic modulus. This trend can also be visualized by observing Figs. 11(a) and (b) in the present study. The variation in the modulus can be attributed to the different levels of stresses induced in the composite with various reinforcements.

The overall strengthening in metal matrix composites is mainly governed by four strengthening mechanisms, i.e., grain refinement, increase in dislocation density by work hardening or thermal mismatch, Orowan strengthening and transfer of load from the matrix to reinforcement. In composites fabricated by friction stir processing with nanoparticles, all the four strengthening mechanisms participate significantly towards the strengthening of the composite.

The ~183% increase in nano-hardness of the Al−SiC mono composite is attributed to the combined effect of grain refinement during FSP, the abrasive behavior of SiC and restriction of dislocation motion by SiC in the matrix. The noteworthy feature is the increase in hardness of Al−SiC composite by ~138% in the present study as compared to the nano-hardness obtained by SHARMA et al [18] using the same process parameters except the SiC particle size and reinforcement strategy. This effect of particle size in enhancing the strength of the composite is also confirmed [35]. The reduction in particle size consequently decreases the grain size by increasing the number of favourite sites for nucleating recrystallization. This phenomenon is in direct conjunction with the Zener−Holloman parameters in metal matrix composites [24]. Also, the SiC particles cause inhomogeneous local deformation, which leads to the break-up of grains and thus assists in grain refinement. The preferential position of the reinforcements during the fabrication of composite is at the grain boundaries. Therefore in the fabricated composite, the SiC particles occupy the preferential grain boundaries and behave as a geometrically necessary dislocation (GND). At the time of composite failure, the dislocations motion in the matrix is restricted by the GND and resists the deformation of the material, thereby causing the strengthening of the composite. The combined effect of these grain refinement and dislocation strengthening along with the hard abrasive behavior of the SiC particles results in the increased surface hardness of the composite as compared to base Al6061 alloy.

The increase in hardness in the case of Al−GNP mono composite is significantly higher than that of Al−CNT mono composites, which is in agreement with the observations made by MAURYA et al [9]. However, the absolute values of hardness in the present study are considerably less than those obtained by MAURYA et al [9]. The higher hardness of Al−GNP and Al−CNT mono composite as compared to as-received Al6061 is attributed to the dislocation generation due to the higher discrepancy in the coefficient of thermal expansion (CTE) between GNP, CNT and Al6061 alloy. The strengthening mechanism of the Al−GNP and Al−CNT mono composites was discussed in detail elsewhere [9].

The hardness of Al−SiC−GNP hybrid composite is increased exceptionally by ~207% and ~43% as compared to base alloy and Al−GNP mono composite respectively. The increase in hardness is attributed to the various phenomena: (1) mechanical exfoliation of GNP, (2) uniform distribution of GNP in the matrix, (3) hardness due to abrasive SiC particles, and (4) significant CTE mismatch between GNP, SiC and Al

matrix. As explained earlier, the presence of SiC leads to the exfoliation of GNP into FLGs (see Fig. 7(b_2)). Due to the wrinkled morphology possessed by these FLGs, the formation of mechanical bonding between FLG and Al matrix is encouraged. Also, the FLGs resist the crack opening/shearing in the matrix during ductile fracture as observed by DIXIT et al [10] and thus strengthened the composite. The GNPs are uniformly distributed in the Al−SiC−GNP hybrid composite. The uniform distribution of GNP contributes to various strengthening mechanisms such as Orowan strengthening and shear lag. With the homogeneous distribution of GNP, the dislocation motion is restricted at an intermittent level and thus resists the composite failure.

Figure 12 confirms the strengthening from the mechanisms as discussed above. Figure 12(a) shows the

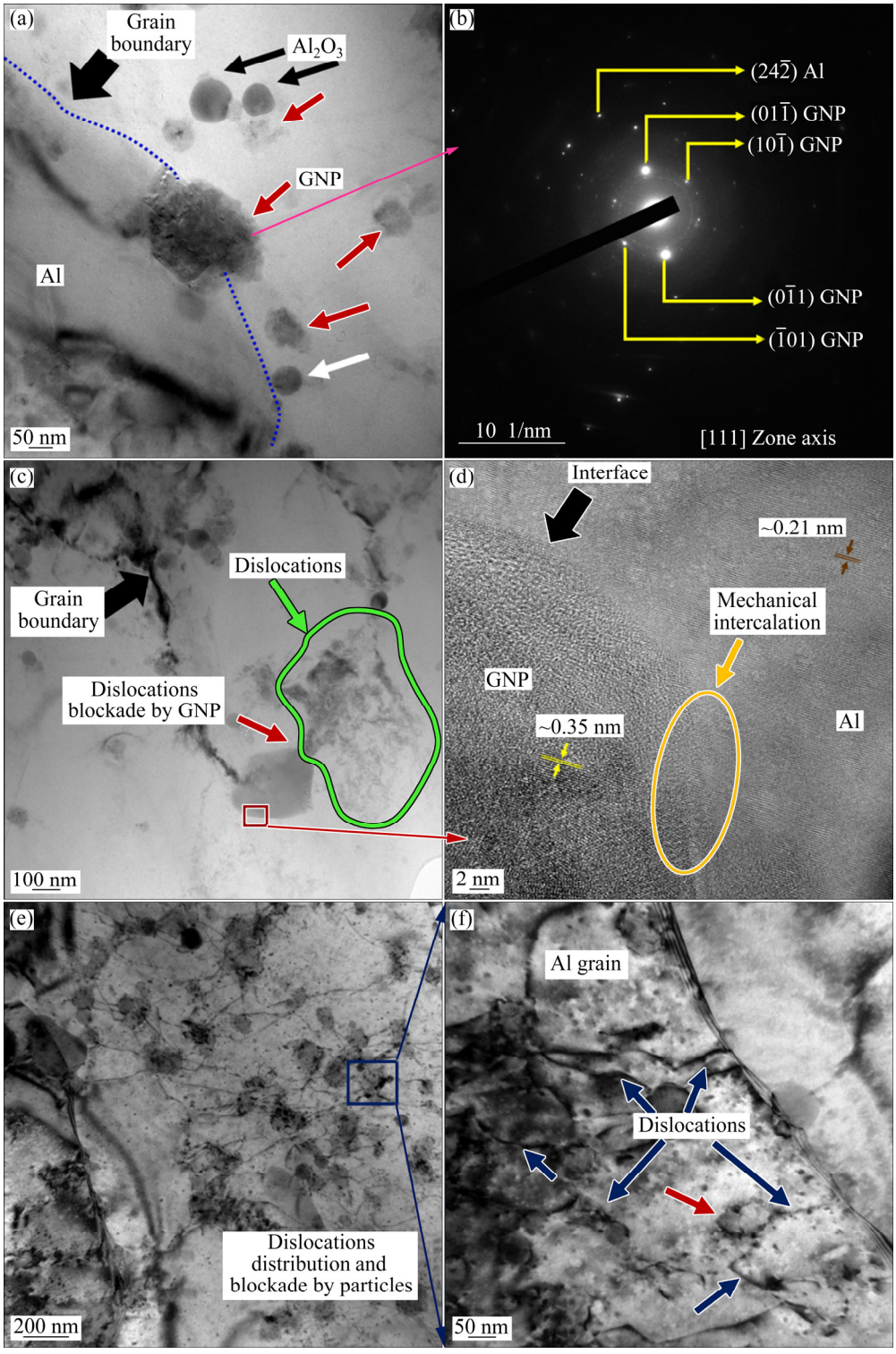

Fig. 12 Bright-field TEM images (a, c−f), SAED pattern (b) of Al−SiC−GNP hybrid composite revealing effects of GNP

GNP particles situated at the grain boundary and thus behaving as GNDs for dislocation motion. The hexagonal shaped diffraction spots in the SAED pattern (see Fig. 12(b)) reveal the six-fold symmetry of carbon atoms arranged in the graphene plane, representing a good crystallinity of the GNP. Figure 12(c) shows another TEM image of the GNP occupying a grain boundary position and thereby restricting the dislocation glide. This phenomenon indicates the contribution of GNP in dislocation strengthening through Orowan strengthening mechanism. Another prominent mechanism for the composite strengthening is the shear lag model which depends upon the load shared by the reinforcement and given by

$$\sigma_{SL} = \sigma_m + v_f \sigma_m \left(\frac{s}{2}\right) \quad (1)$$

where σ_{SL} is the yield strength from the shear lag model, s is the aspect ratio of GNP (0.177 for wrinkled graphene), σ_m is the yield strength of the Al matrix, and v_f is the GNP volume fraction.

In the shear lag model, the transfer of tensile strength from the matrix to GNP in the form of interfacial shear stress mainly depends upon the interfacial bonding between the Al matrix and GNP. Figure 12(d) represents the high magnification TEM image, revealing the interface of the Al matrix and GNP. The Al−GNP interface is clean and free from any defects like microvoids, cracks, inclusions, etc. Also, a transition zone (encircled) indicates the intercalation between the atoms of carbon and aluminium. The existence of a transition zone reveals the strong bonding between aluminium and GNP. This strongly bonded aluminium matrix and GNP confirm the significant contribution of the load sharing mechanism in the overall strengthening of the composite. The interlayer spacings (d) of GNP and aluminium are found to be ~0.35 nm and 0.21 nm, respectively. Figures 12(e) and (f) show the dislocation distribution and its blockade by several reinforcement particles, which further confirms the dislocation strengthening in the composite.

Figure 13 shows the TEM images of the Al−SiC−GNP composite from the perspective of SiC. Figure 13(a) shows the SiC particles occupied at the grain boundary similar to GNP as discussed earlier. The characteristic SAED pattern shown in Fig. 13(b), confirms the identified particles as SiC. The interfacial bond strength of SiC with the Al matrix is analyzed through the high magnification image, as shown in Fig. 13(c). Similar to GNP, here also a perfect interface free from any defects such as micro voids, cracks, inclusions, etc. is obtained. Also, excellent intercalation is observed between the atoms of SiC and aluminium as shown by the encircled region. Further, the GATAN microscopy graph (Fig. 13(e)) reveals that the interlayer distance between the atoms is ~0.26 nm, which is close to that observed for SiC by various researchers [40]. Figure 13(d) reveals an exciting feature of the Al−SiC−GNP composite. The high flow shear stresses generated during FSP lead to exfoliation of GNP. When these GNP particles are located in the periphery of SiC, a thin layer of GNP makes bonding with SiC and acts as a bridge between the two particles as shown in Fig. 13(d) (inset). This bridging tendency is also observed by SHARMA et al [27] and extensively favors the corrosion resistance by reducing the interfacial corrosion between SiC and aluminium matrix. Also, apart from corrosion resistance, this bridging effect significantly contributes to the load sharing during loading, and consequently, enhances the composite performance. Figure 13(d) also shows the dislocations blockade by the SiC particles.

The hard abrasive behavior of the SiC particles also contributes significantly to the strengthening of the composite. Apart from the hard abrasive behavior, the SiC and GNP both contribute towards the increased grain refinement due to pinning action at the grain boundaries. Also, the effect of grain boundary pinning intensified due to the nano-sized GNPs as explained earlier in this section. The last and the foremost reason for the higher hardness of the Al−SiC−GNP composite is the existence of large mismatch between the CTEs of Al matrix (~2.71×10^{-5} K^{-1}), SiC (~4.2×10^{-6} K^{-1}) and GNP (~−9×10^{-6} K^{-1}). This higher discrepancy between the CTEs leads to the entrapment of residual compressive stresses in the composite, and consequently, the strength of the composite increases.

The load−displacement curve (Fig. 11(b)) shows some key noteworthy features in GNP based composites. (1) In Al−GNP mono composite, the unloading curve shows a steep decrease in load up to ~3000 μN, and afterward, the penetration depth decreases steeply. This behaviour may be attributed to the higher stiffness of the GNP due to which, the indenter retracts slowly up to threshold limit and afterward a sudden unloading takes place; (2) In Al−SiC−GNP composite, during loading the load increases gradually up to ~750 μN and after that there is a steep increase in the load. This phenomenon is attributed to the de-bonding of Al−GNP mechanical bonding, which is shown by the pop-in (encircled). The similar feature is also observed during the loading of Al−GNP mono composite.

The hardness of Al−SiC−CNT hybrid composite increases by ~27% and ~15% as compared to as-received Al6061 alloy and Al−CNT mono composite respectively. The 15% increase in hardness of Al−SiC−CNT hybrid composite as compared to Al−CNT mono composite is attributed to the absence of CNT clusters. The presence

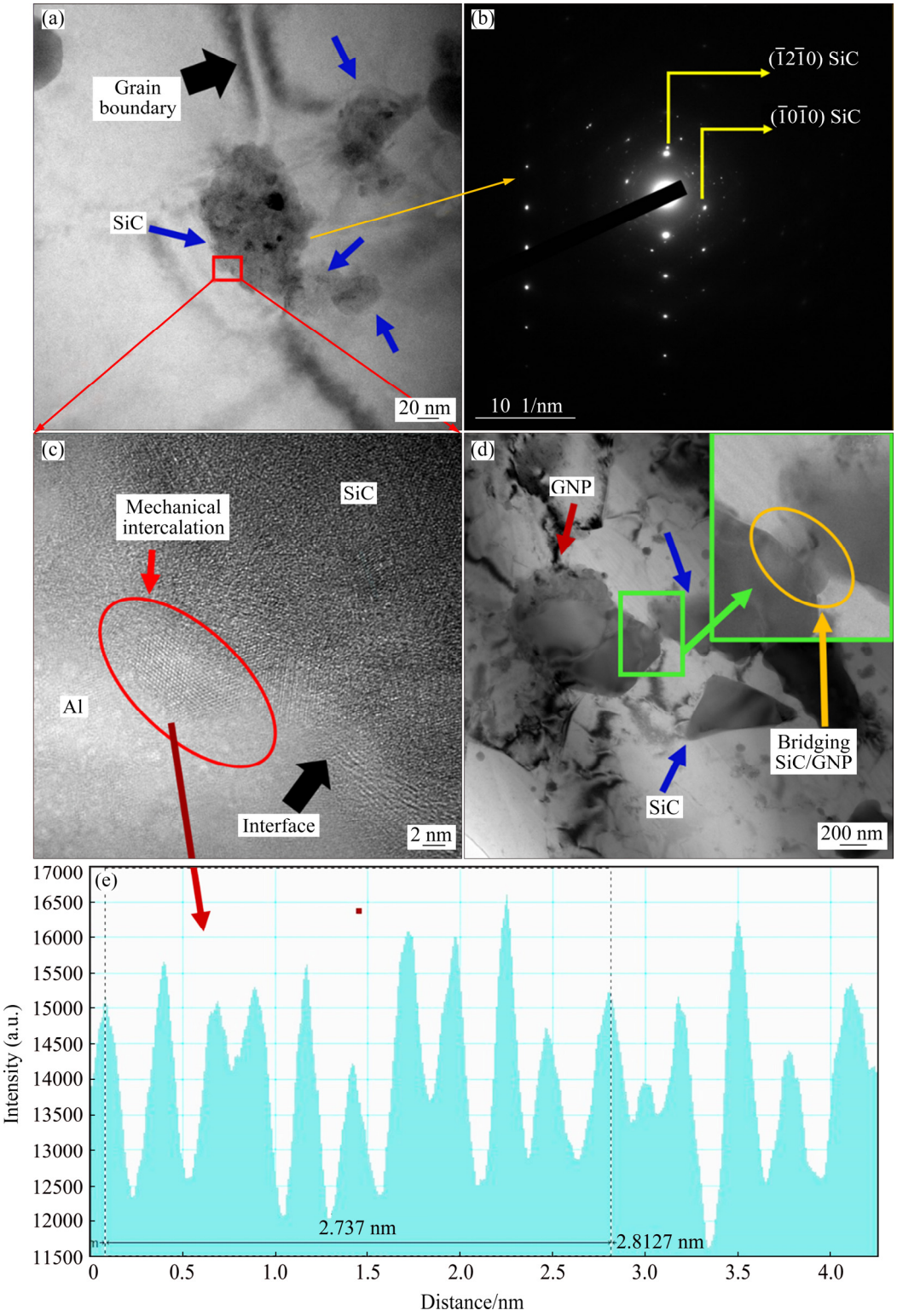

Fig. 13 Bright-field HR-TEM images (a, c, d), SAED pattern (b) and GATAN plot (e) of Al−SiC−GNP hybrid composite revealing effect of SiC

of CNT clusters in mono composites deteriorates the hardness and modulus because of the inability to bear the load and relatively easy induction of stress concentration and microvoid nucleation, whereas, the single dispersed CNT in Al−SiC−CNT hybrid composite shares the load effectively and resists the void formation as shown in Fig. 14(a). The noteworthy feature in the hybrid composite is the lower hardness of the Al−SiC−CNT hybrid composite as compared to Al−SiC−GNP hybrid composite. This behavior is attributed to the decrease in CTE difference in Al−SiC−CNT hybrid composite due to increase in CTE of CNT (~2×10^{-5} K^{-1}). The thermal

mismatch also decreases the magnitude of compressive residual strain experienced by the composite leading to the decrease in overall hardness and modulus of the composite.

For predicting the nanomechanical behavior of the fabricated surface composites, the maximum load applied is 5000 μN, and the maximum indentation depth achieved is ~600 nm for all the samples. Thus, the nanoindentation study reveals the mechanical properties only in this regime (<1 μm). However, the overall performance of the composites can only be predicted by taking both bulk and surface properties into consideration, Thus, to analyze the bulk properties of the fabricated composites, Vickers microhardness test was carried out on the cross section of the samples obtained transverse to the FSP direction. Figure 15(a) shows the variation of microhardness for as-received Al6061 alloy, unreinforced processed aluminium and various fabricated composites as a function of distance from the center of the stir zone. All the fabricated composites and processed Al show a higher hardness in the stir zone with the maximum being in Al−GNP−SiC hybrid composite. The microhardness values show a similar trend as that of nanoindentation for various fabricated composites, as shown in Fig. 15(b). Thus, it can be concluded that the strengthening mechanisms similar to the nanohardness also contribute towards the higher microhardness of the composites.

The hardness values (both micro and nano-hardness) obtained in Al−SiC-GNP/MWCNT are significantly higher than the obtained values of Al−SiC−graphite by SHARMA et al [18] with a maximum in Al−SiC-GNP. Thus, for the Al6061 alloy hybrid composite containing SiC, the GNP will be the best reinforcement in the carbonaceous family for increasing the surface hardness.

3.6 Coefficient of friction (COF) and specific wear rate

Figures 16(a) and (b) present the variation in COF over time and specific wear rate of as-received Al6061 alloy and hybrid composites in dry sliding wear conditions at room temperature, respectively. As shown in Fig. 16(a), the COF corresponding to the as-received Al6061 alloy is above 0.5 with severe fluctuation during the wear test. Whereas, the COF is the most stable and minimum (~0.4) in Al−SiC−GNP hybrid composite as compared to ~0.5 in Al−SiC−CNT hybrid composite. The specific wear rate (Fig. 16(b)) of as-received Al6061 alloy and hybrid composites are calculated by

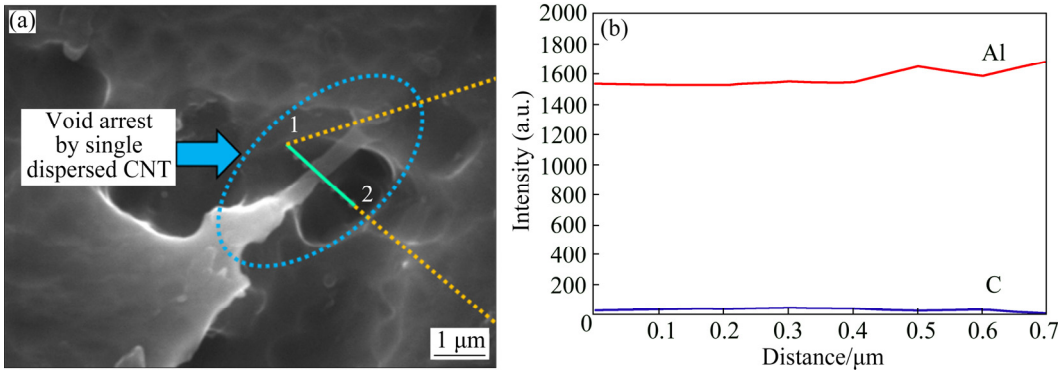

Fig. 14 SEM image of Al−SiC−CNT hybrid composite (a) and EDAX analysis of lines 1−2 in (a)

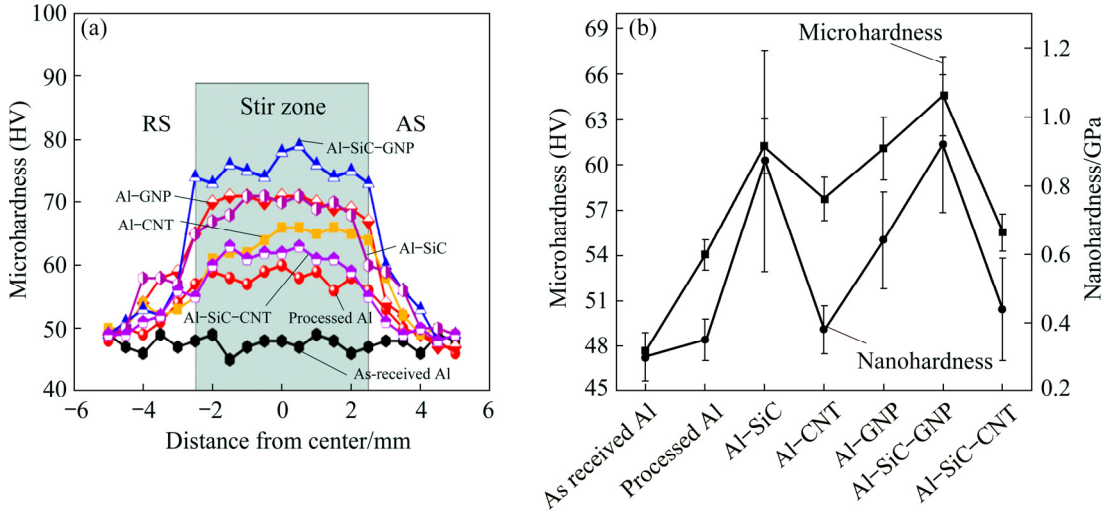

Fig. 15 Vickers microhardness plot (a) and comparison of average nano and microhardness for various composites (b)

Archard equation [41]. The specific wear rate decreased by ~56% in Al−SiC−GNP while it increased by ~122% in Al−SiC−CNT hybrid composite as compared to the as-received Al6061 alloy. The detailed analysis of wear mechanism is discussed through observation of worn surface morphology in the subsequent section.

3.7 Worn surface morphology

3.7.1 As-received Al6061

Figures 17(a−e) depict the surface morphologies of as-received Al6061 alloy after dry sliding wear test. Figure 17(a) represents the low magnification image to visualize the overall worn surface and a track width of the material. Figure 17(b) shows the high magnification

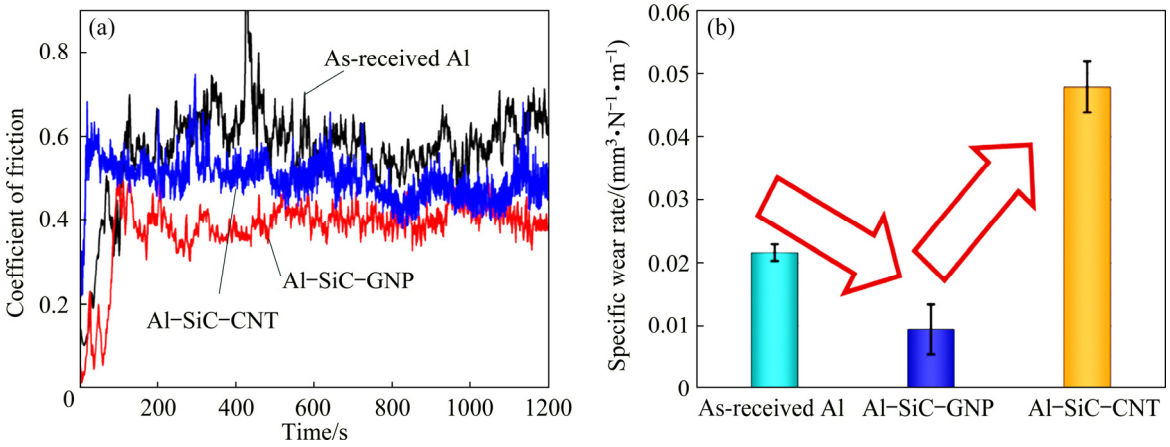

Fig. 16 Variation in coefficient of friction (a) and specific wear rate (b) of as-received Al6061 alloy and hybrid composites

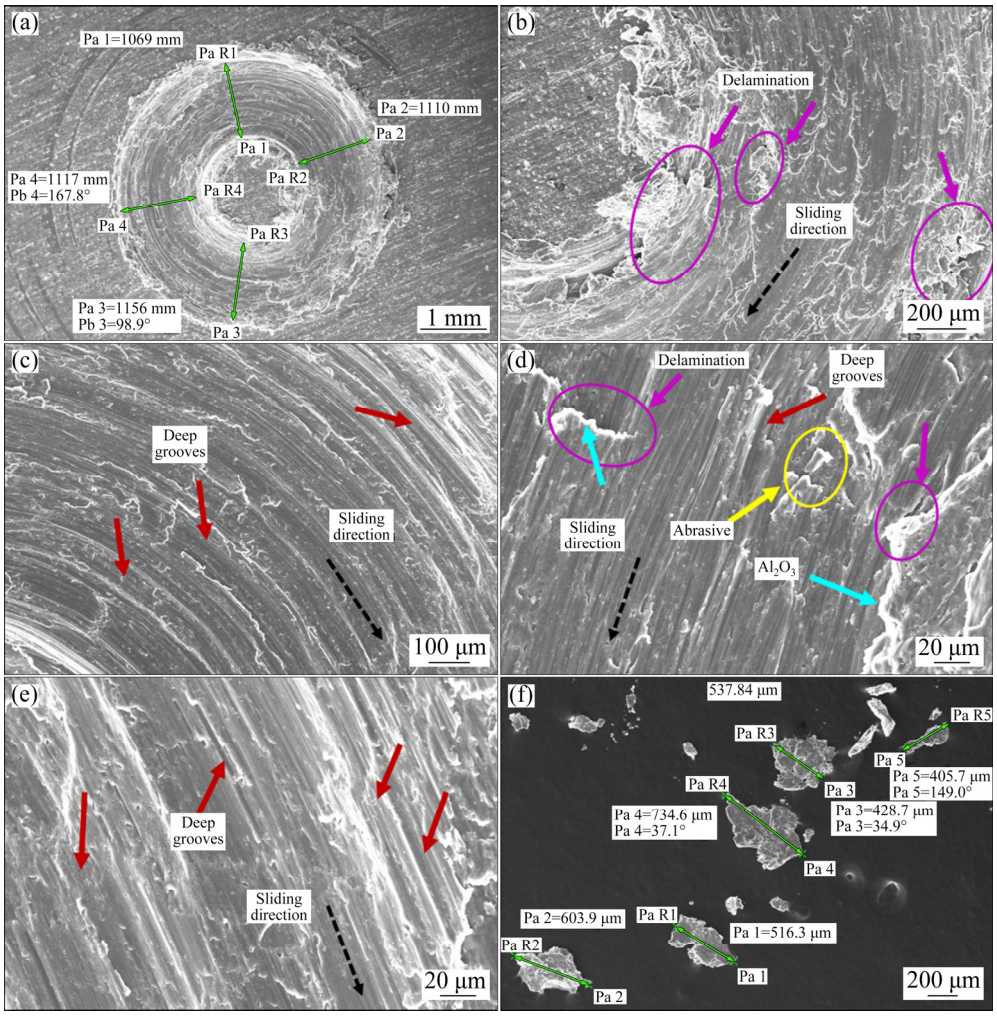

Fig. 17 SEM micrographs of worn surface (a−e) and debris (f) of as-received Al6061 alloy

SEM micrograph depicting the delamination of the material on the wear track by the counter steel part. The delamination behavior is severe, as shown by the encircled regions. The presence of delamination of the material indicates the existence of adhesion as the wear mechanism. During the wear testing, a localized adhesion between the aluminium and counter steel takes place. This localized adhesion is immediately followed by its breakdown due to the work hardening of surface and subsurface regions. This breakdown results in the initiation of cracks in the sub-surface region. As time progresses, these cracks further propagate and get interconnected and finally results in the removal of the surface layer in the form of sheets or flakes. Figure 17(c) reveals the presence of parallel and concentric grooves on the wear track. These grooves indicate the abrasion component of the wear mechanism. Thus, both abrasion and adhesion wear mechanisms are present in the case of as-received Al6061 alloy. Figure 17(d) shows the bright region on the wear track. According to SAHOO et al [42], these bright contrast region corresponds to the formation of Al_2O_3 due to the reaction of aluminium with atmospheric oxygen in the presence of frictional heating. This Al_2O_3 is abrasive and engages between the steel counterpart and aluminium. This phenomenon further expedites the delamination of the as-received Al6061 alloy. Figure 17(e) shows the deep grooves along the sliding direction. The existence of both abrasion and adhesion mechanism is confirmed by the worn surface analysis. However, the dominant mechanism cannot be concluded from these micrographs. The SEM micrograph of debris generated after the wear test is shown in Fig. 17(f). The large and flaky debris of average size ~537.84 μm is observed. The removal of material in the form of such large flakes indicates adhesion as the dominant wear mechanism in the as-received Al6061 alloy.

3.7.2 Al−SiC−GNP hybrid composite

Figures 18(a−e) show the SEM images of the worn surface after wear test of Al−SiC−GNP hybrid composite. Figures 18(f) and (g) show the EDS profile obtained from the corresponding section, whereas, Fig. 18(h) represents the SEM micrograph of the debris generated during the wear test. As compared to worn morphology of the as-received Al6061 alloy in Fig. 17(a), the surface morphology visualized in Fig. 18(a) is clean and consists of less delaminated patches. Figure 18(b) reveals the shallow grooves and delaminated patches on the wear track. The presence of grooves again indicates the abrasive wear during sliding, which leads to the exposure of GNP to the surface. Figure 18(c) represents the shallow grooves with a clean surface (without any abrasive/debris). Figure 18(d) represents the GNP embedded in the Al matrix, which is being pulled out to the surface by the abrasive rubbing of the steel counterpart. Also, the wrinkled morphology of the GNP is still retained after the plastic deformation and frictional heating during dry sliding wear. The peak corresponding to carbon in the point EDS analysis (see Fig. 18(f)) confirms the wrinkled particle as a GNP. Figure 18(e) reveals the tribolayer formed on the surface by the shearing of GNP under plastic deformation during the wear test. The size of tribolayer formed in Al−SiC−GNP hybrid composite is considerably larger than that obtained by Al−SiC−CNT (discussed later in the manuscript) hybrid composite. KURT et al [43] have also observed a similar lubrication effect during the wear test of Al−TiC−Al_2O_3 hybrid composite. The existence of broad and consistent GNP tribolayer is attributed to the large specific area possessed by the GNPs. Due to this larger specific area, the squeezing out of the graphene layer is relatively easy. According to previous research, the metal around wide dispersed particles in the tribo-surface and subsurface region was easily plastically deformed during sliding. As a result, the high specific area possessed GNP particles was preferentially squeezed onto the surface and tended to extend in a larger area on the surface by the shearing and, thus, smeared between the mating surfaces. The line EDS analysis over the GNP tribolayer is displayed in Fig. 18(g). The line spectrum reveals the presence of carbon along with oxygen on the tribo surface. The presence of oxygen is may be due to the formation of aluminium oxide, which was also observed by various researchers in the past [41]. This tribolayer has previously been reported to impede direct contact between the friction pair, thus reducing COF and wear rate. Shallow scratches can also be observed, which can be produced by abrasive particles obtained from the aluminium oxide. It should be noted that the existence of scratches and craters due to the lubrication effect of GNP is reduced to a larger extent.

Finally, the addition of GNP along with SiC improves the wear behavior of the hybrid composite due to its self-lubricating mechanism, i.e., the smearing out of graphene particles on the surface in the form of tribolayer. Moreover, the GNP improves the load-bearing capacity of the matrix through the excellent Al/GNP interface (Fig. 12(d)), which further increases its wear resistance ability. The excellent solid lubricant effect possessed by the GNPs is attributed to:

(1) The layered structure of GNP which provides it with transportable flake shape along with very less adhesion to the surface;

(2) The higher specific surface area of the GNP flakes due to which it spreads like a film instead of getting arrested in the surface asperities;

(3) The wrinkled and folded morphology which

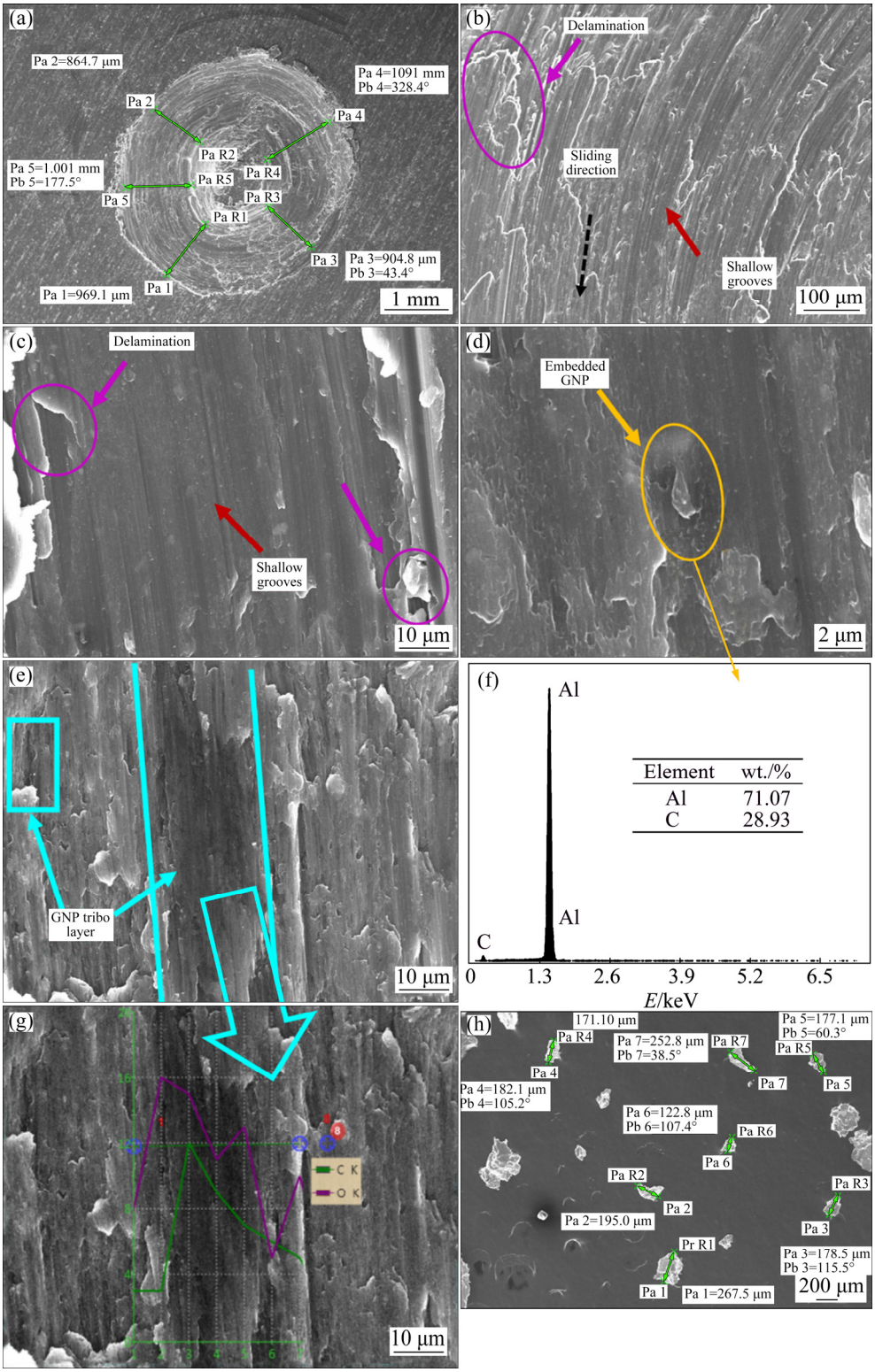

Fig. 18 SEM images of worn surface (a−e), EDS analysis (f) of region in (d), line EDS mapping (g) of region in (e), SEM image (h) of post wear debris of Al−SiC−GNP hybrid composite

behaves like a source of stress dissipation during loading.

The wear debris generated after the dry sliding behavior of the Al−SiC−GNP hybrid composite (Fig. 18(h)) also reveals small particles with flaky morphology. The debris particle is reduced from ~537 μm in as-received Al6061 alloy to ~171 μm in Al−SiC−GNP hybrid composite. The reduced size of debris corresponds to the transition of wear mechanism from adhesion in the as-received Al6061 alloy to abrasion in the hybrid composite.

3.7.3 Al−SiC−CNT hybrid composite

Figures 19(a−e) show the SEM micrographs of the worn surface after wear test of Al−SiC−CNT hybrid composite. Figure 19(a) shows the overall worn surface morphology of the composite. Figure 19(b) reveals the presence of relatively wide and pretty deep relentless grooves with intermittent parallel fringes; delamination effect and micro-size wear debris on the wear track. On the wear track, plastic deformation at the edges of the grooves can also be visualized. The unstable and high COF of the Al−SiC−CNT hybrid composite as compared to Al−SiC−GNP suggests that the shape of carbon is responsible for the alteration of Al−SiC−X hybrid composites wear mechanism. During the thermo-mechanical processing, CNT particles were mechanically damaged, which was seen in Fig. 8. The CNTs were shortened with a damaged tube-like structure. Also, the distribution of residual thermal stresses due to the CTE difference between the Al matrix, SiC, and CNT will largely depend upon the morphology, the size and the volume of CNT. The addition of CNT in the Al−SiC composite was expected to affect the friction and wear behavior by forming a steady and lubricated transfer film between the sliding surfaces as previously observed in GNP-enhanced SiC composites. However, due to the tubular morphology possessed by the CNTs, the particles get rolled, which leads to three body mechanism instead of shearing and squeezing out in the form of layers. In the absence of the protective layer between the substrate and steel counterface, under the cyclic loading, delamination takes place as seen in Fig. 19(b). In the absence of a continuous carbonaceous layer, the direct contact of steel counterpart to the composite also takes place which results in the formation of deep grooves, as shown in Fig. 19(c). Figure 19(d) represents the discontinuous smeared CNT on the surface of the composite. Also, some subsurface CNTs ready to be pulled out on the surface can be visualized.

The significant effect of CNT smearing can also be visualized via the presence of a smooth surface or shallow groves near the smeared out CNTs. The smooth surface is a direct indication of the wear resistance

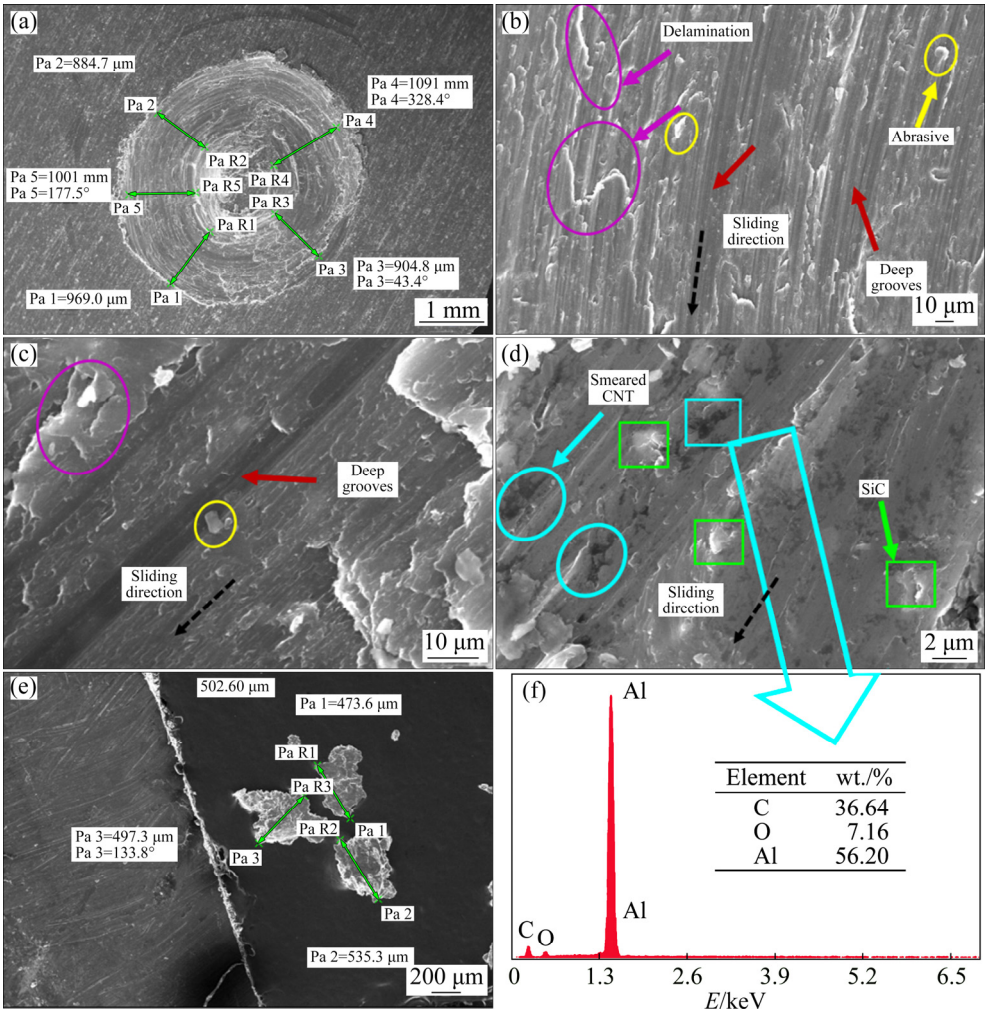

Fig. 19 SEM images of worn surface (a−d), post wear debris (e) of Al−SiC−CNT hybrid composite, EDS analysis (f) of region shown in (d)

provided by the tribo layer formed on the surface. Figure 19(f) represents the point EDS analysis obtained on the dark patches shown in Fig. 19(d). The presence of carbon confirms the dark patches as the squeezed out inconsistent tribolayer on the wear track. Another vital information obtained from the SEM micrograph shown in Fig. 19(d), is the existence of a rough surface in the sliding track consisting of pull out SiC from the subsurface region. The rough surface morphology can be attributed to: (1) the breakage of the formed tribo layer by the abrasive SiC particle; (2) the hard abrasion mechanism provided by the SiC particles on the surface. Though a considerable amount of information is provided by the SEM micrographs of the wear track, a clear indication of the wear mechanism is stated by the study of debris generated during the wear. As seen in Fig. 19(e) the debris size is increased from ~171 μm in Al−SiC−GNP composite to ~502.60 μm in Al−SiC−CNT composite. The removal of the composite surface in the form of large debris confirms the adhesion as the predominant wear mechanism. Also, the increased wear rate and COF support the discussion. The absence of a continuous carbonaceous layer and the presence of SiC (which further acts as the abrasive when detached from the matrix by the steel counterpart) increase the overall wear rate of the composite as compared to the as-received Al6061alloy.

4 Conclusions

(1) Thermal history shows that the peak temperature observed in various fabricated composites is well below the melting point of aluminium alloy and thus confirms the solid-state plastic deformation during FSP. Also, the higher cooling rate of GNP based composites up to a certain threshold temperature is attributed to the excellent thermal conductivity of GNP.

(2) The cluster of GNPs and CNTs are visualized in Al−GNP and Al−CNT mono composites, respectively. However, in Al−SiC−GNP hybrid composite the GNP distribution is homogeneous along with the mechanical exfoliation of GNP to FLG in the presence of SiC. The Al−SiC−CNT composite shows some single dispersed CNT with the damaged ends. Also, the CNT shortening takes place due to flow shear stress experienced during FSP.

(3) The absence of intermetallic compounds is observed by X-ray diffraction and is attributed to the insufficient heat generation, which is necessary for the initiation of the kinetics of intermetallic compound formation.

(4) The increase in defect density and exfoliation of GNP to FLG in Al−SiC−GNP is confirmed from Raman spectroscopy. The peak shift of Raman bands indicates towards the strain experienced by the reinforcement particles. Raman spectrum of Al−SiC−CNT confirms the delamination of the tube walls.

(5) Al−SiC−GNP and Al−SiC−CNT hybrid composites reveal ~36% and ~17% higher microhardness than the as-received Al6061 alloy.

(6) The nano-hardnesses of Al−SiC−GNP and Al−SiC−CNT hybrid composite are increased by ~207% and ~27% as compared to the as-received Al6061 alloy. The maximum hardness of the Al−SiC−GNP hybrid composite is mainly attributed to the mechanical exfoliation of GNP, and the large thermal mismatch between Al, GNP, and SiC particles. Various mechanisms like Orowan strengthening, load sharing, and grain refinement are significantly responsible for the strengthening of the composites.

(7) A perfect defect-free interface between the Al matrix and GNP is observed by TEM. The bridging phenomenon between SiC and GNP due to shearing of GNP layers is also confirmed. The dislocation blockade by SiC and GNP is also observed.

(8) Tribological assessment reveals the ~56% decrease in specific wear rate of Al−SiC−GNP hybrid composite whereas it increases by ~122% in Al−SiC−CNT hybrid composite relative to the as-received Al6061 alloy. The formation of tribolayer owing to the squeezed out GNP on the surface is responsible for the improved tribological performance of Al−SiC−GNP hybrid composite

(9) The Al−SiC−GNP hybrid composite is concluded to be the best one in the Al−SiC−carbonaceous compound family of hybrid composites for increasing the surface hardness and wear resistance of aluminium alloys.

References

[1] JIANG X, WANG N, ZHU D. Friction and wear properties of in-situ synthesized Al_2O_3 reinforced aluminum composites [J]. Transactions of Nonferrous Metals Society of China, 2014, 24: 2352–2358.

[2] AKHTAR F, GUO S. Development of Si_3N_4/Al composite by pressureless melt infiltration [J]. Transactions of Nonferrous Metals Society of China, 2006, 16: 629−632.

[3] ERDEMIR F, CANAKCI A, VAROL T. Microstructural characterization and mechanical properties of functionally graded Al2024/SiC composites prepared by powder metallurgy techniques [J]. Transactions of Nonferrous Metals Society of China, 2015, 25: 3569−3577.

[4] MOSES J J, DINAHARAN I, SEKHAR S J. Prediction of influence of process parameters on tensile strength of AA6061/TiC aluminum matrix composites produced using stir casting [J]. Transactions of Nonferrous Metals Society of China, 2016, 26: 1498−1511.

[5] AMRA M, RANJBAR K, HOSSEINI S A. Microstructure and wear performance of Al5083/CeO_2/SiC mono and hybrid surface composites fabricated by friction stir processing [J]. Transactions of Nonferrous Metals Society of China, 2018, 28: 866−878.

[6] CHOI D H, KIM Y I, KIM D U, JUNG S B. Effect of SiC particles

on microstructure and mechanical property of friction stir processed AA6061-T4 [J]. Transactions of Nonferrous Metals Society of China, 2012, 22: s614–18.

[7] JANBOZORGI M, SHAMANIAN M, SADEGHIAN M, SEPEHRINIA P. Improving tribological behavior of friction stir processed A413/SiC_p surface composite using MoS_2 lubricant particles [J]. Transactions of Nonferrous Metals Society of China, 2017, 27: 298−304.

[8] JEON C H, JEONG Y H, SEO J J, TIEN HN, HONG S T, YUM Y J, HUR S H, LEE K J. Material properties of graphene/aluminum metal matrix composites fabricated by friction stir processing [J]. International Journal of Precision Engineering and Manufacturing, 2014, 15: 1235−1239.

[9] MAURYA R, KUMAR B, ARIHARAN S, RAMKUMAR J, BALANI K. Effect of carbonaceous reinforcements on the mechanical and tribological properties of friction stir processed Al6061 alloy [J]. Materials and Design, 2016, 98: 155−166.

[10] DIXIT S, MAHATA A, MAHAPATRA D R, KAILAS S V, CHATTOPADHYAY K. Multi-layer graphene reinforced aluminum —Manufacturing of high strength composite by friction stir alloying [J]. Composites Part B: Engineering, 2018, 136: 63−71.

[11] KHODABAKHSHI F, ARAB S M, ŠVEC P, GERLICH A P. Fabrication of a new Al−Mg/graphene nanocomposite by multi-pass friction-stir processing: Dispersion, microstructure, stability, and strengthening [J]. Materials Characterization, 2017, 132: 92−107.

[12] LIU Z Y, XIAO B L, WANG W G, MA Z Y. Singly dispersed carbon nanotube/aluminum composites fabricated by powder metallurgy combined with friction stir processing [J]. Carbon, 2012, 50: 1843−1852.

[13] IZADI H, GERLICH A P. Distribution and stability of carbon nanotubes during multi-pass friction stir processing of carbon nanotube / aluminum composites [J]. Carbon, 2012, 50(12): 4744−4749.

[14] LIU Q, LIMING K, LIU F, HUANG C, XING L. Microstructure and mechanical property of multi-walled carbon nanotubes reinforced aluminum matrix composites fabricated by friction stir processing [J]. Materials & Design, 2013, 45: 343−348.

[15] LIM D K, SHIBAYANAGI T, GERLICH A P. Synthesis of multi-walled CNT reinforced aluminium alloy composite via friction stir processing [J]. Materials Science and Engineering A, 2009, 507: 194−199.

[16] RAJMOHAN T, PALANIKUMAR K, RANGANATHAN S. Evaluation of mechanical and wear properties of hybrid aluminium matrix composites [J]. Transactions of Nonferrous Metals Society of China, 2013, 23: 2509−2517.

[17] DEVARAJU A, KUMAR A, KOTIVEERACHARI B. Influence of addition of Gr_p/Al_2O_{3p} with SiC_p on wear properties of aluminum alloy 6061-T6 hybrid composites via friction stir processing [J]. Transactions of Nonferrous Metals Society of China, 2013, 23: 1275−1280.

[18] SHARMA A, SHARMA V M, MEWAR S, PAL S K, PAUL J. Friction stir processing of Al6061-SiC-graphite hybrid surface composites [J]. Materials and Manufacturing Processes, 2018, 33: 795−804.

[19] TANG X C, MENG L Y, ZHAN J M, JIAN W R, LI W H, YAO X H, HAN Y L. Strengthening effects of encapsulating graphene in SiC particle-reinforced Al-matrix composites [J]. Computational Materials Science, 2018, 153: 275−281.

[20] ZENG X, YU J, FU D, ZHANG H, TENG J. Wear characteristics of hybrid aluminum-matrix composites reinforced with well-dispersed reduced graphene oxide nanosheets and silicon carbide particulates [J]. Vacuum, 2018, 155: 364−375.

[21] ŞENEL M C, GÜRBÜZ M, KOÇ E. Fabrication and characterization of synergistic Al−SiC-GNPs hybrid composites [J]. Composites Part B: Engineering, 2018, 154: 1−9.

[22] ZHAN J M, JIAN W R, TANG X C, HAN Y L, LI W H, YAO X H, MENG L Y. Tensile deformation of nanocrystalline Al-matrix composites: Effects of the SiC particle and graphene [J]. Computational Materials Science, 2019, 156: 187−194.

[23] HEKNER B, MYALSKI J, VALLE N, BOTOR-PROBIERZ A, SOPICKA-LIZER M, WIECZOREK J. Friction and wear behavior of Al−SiC(n) hybrid composites with carbon addition [J]. Composites Part B: Engineering, 2017, 108: 291−300.

[24] SHARMA A, SHARMA V M, SAHOO B, PAL S K, PAUL J. Effect of multiple micro channel reinforcement filling strategy on Al6061-graphene nanocomposite fabricated through friction stir processing [J]. Journal of Manufacturing Processes, 2019, 37: 53−70.

[25] KHAN N Z, SIDDIQUEE A N, KHAN Z A, SHIHAB S K. Investigations on tunneling and kissing bond defects in FSW joints for dissimilar aluminum alloys [J]. Journal of Alloys and Compounds, 2015, 648: 360−367.

[26] MISHRA R S, MA Z Y, CHARIT I. Friction stir processing: A novel technique for fabrication of surface composite [J]. Materials Science and Engineering A, 2003, 341: 307−310.

[27] SHARMA A, SHARMA V M, SAHOO B, JOSEPH J, PAUL J. Study of nano-mechanical, electrochemical and raman spectroscopic behavior of Al6061-SiC-graphite hybrid surface composite fabricated through friction stir processing [J]. Journal of Composites Science, 2018, 2: 32.

[28] ZHANG D, SUGIO K, SAKAI K, FUKUSHIMA H, YANAGISAWA O. Effect of volume fraction on the flow behavior of Al−SiC composites considering the spatial distribution of delaminated particles [J]. Materials Transactions, 2008, 49: 661−670.

[29] CHOI H J, BAE D H. Strengthening and toughening of aluminum by single-walled carbon nanotubes [J]. Materials Science and Engineering A, 2011, 528: 2412−2417.

[30] BASTWROS M M H, ESAWI A M K, WIFI A. Friction and wear behavior of Al−CNT composites [J]. Wear, 2013, 307: 164−173.

[31] SAHOO B, PAUL J. Solid state processed Al-1100 alloy/MWCNT surface nanocomposites [J]. Materialia, 2018, 2: 196−207.

[32] SAHOO B, JOSEPH J, SHARMA A, PAUL J. Surface modification of aluminium by graphene impregnation [J]. Materials and Design, 2017, 116: 51−64.

[33] SAHOO B, KUMAR R, JOSEPH J, SHARMA A, PAUL J. Preparation of aluminium 6063-graphite surface composites by an electrical resistance heat assisted pressing technique [J]. Surface and Coatings Technology, 2017, 309: 563−572.

[34] ZHANG Z W, LIU Z Y, XIAO B L, NI D R, MA Z Y. High efficiency dispersal and strengthening of graphene reinforced aluminum alloy composites fabricated by powder metallurgy combined with friction stir processing [J]. Carbon, 2018, 135: 215−223.

[35] SAHOO B, JOSEPH J, SHARMA A, PAUL J. Particle size and shape effects on the surface mechanical properties of aluminium coated with carbonaceous materials [J]. Journal of Composite Materials, 2019, 53: 261−270.

[36] SHARMA A, SAGAR S, MAHTO R P, SAHOO B, PAL S K, PAUL J. Surface modification of Al6061 by graphene impregnation through a powder metallurgy assisted friction surfacing [J]. Surface and Coatings Technology, 2018, 337: 12−23.

[37] STADELMANN R, HUGHES B, ORLOVSKAYA N, GRASSO S, REECE M J. 2D Raman mapping and thermal residual stresses in SiC grains of ZrB2−SiC ceramic composites [J]. Ceramics International, 2015, 41: 13630−13637.

[38] SHARMA A, NARSIMHACHARY D, SHARMA V M, SAHOO B, PAUL J. Surface modification of Al6061-SiC surface composite through impregnation of graphene, graphite & carbon nanotubes via FSP: A tribological study [J]. Surface and Coatings Technology,

2019, 368: 175−191.
[39] SAHOO B, GIRHE S D, PAUL J. Influence of process parameters and temperature on the solid state fabrication of multilayered graphene-aluminium surface nanocomposites [J]. Journal of Manufacturing Processes, 2018, 34: 486−494.
[40] NUTT S R, WAWNER F E. Silicon carbide filaments: Microstructure [J]. Jouranl of Materials Science, 1985, 20: 1953−1960.
[41] SAHOO B, NARSIMHACHARY D, PAUL J. Tribological behavior of solid-state processed Al-1100/GNP surface nanocomposites [J]. Journal of Materials Engineering and Performance, 2018, 27: 6529−6544.
[42] SAHOO B, NARSIMHACHARY D, PAUL J. Surface mechanical and self-lubricating properties of MWCNT impregnated aluminium surfaces [J]. Surface Engineering, 2019: 1−12.
[43] KURT H I, ODUNCUOGLU M, ASMATULU R. Wear behavior of aluminum matrix hybrid composites fabricated through friction stir welding process [J]. Journal of Iron and Steel Research International, 2016, 23: 1119−1126.

搅拌摩擦加工制备石墨烯和碳纳米管增强 Al6061−SiC 复合材料的显微组织演变及表面性能

Abhishek SHARMA, Vyas Mani SHARMA, Jinu PAUL

Department of Mechanical Engineering, Indian Institute of Technology, Kharagpur 721302, India

摘　要：对比研究多壁碳纳米管(CNT)和石墨烯纳米片(GNP)对 Al−SiC 基复合材料表面性能的影响，用搅拌摩擦法分别制备 Al−SiC−CNT 和 Al−SiC−GNP 复合材料。显微组织表征表明，与 CNTs 相比，GNPs 在铝基体中的分散更加均匀。此外，还观察到 SiC 和 GNP 颗粒对位错的阻碍以及基体与增强材料之间的无缺陷界面。纳米压痕结果表明，与 Al6061 合金相比，Al−SiC−GNP 和 Al−SiC−CNT 复合材料的表面纳米硬度分别显著提高约 207% 和 27%，显微硬度分别提高了约 36% 和 17%。摩擦学分析表明，Al−SiC−GNP 复合材料的比磨损率降低约 56%，而 Al−SiC−CNT 复合材料的比磨损率提高约 122%。Al−SiC−GNP 复合材料的高强度是由于在 SiC 存在下，GNPs 会机械剥离成几层石墨烯(FLG)。此外，热失配、晶粒细化和 Orowan 循环等多种机制对复合材料的增强也有重要作用。而摩擦性能提升的主要原因是其表面挤出的 GNP 形成摩擦层，拉曼光谱和其他表征方法证实这一结果。

关键词：搅拌摩擦加工；石墨烯；碳纳米管；复合材料；磨损

(Edited by Xiang-qun LI)